Supplementary Information for

Nano-geometric deformation synergistic Co nanoparticles&Co-N_4 composite site for proton exchange membrane fuel cells

Xiaoyang Cheng[a], Jian Yang[a]*, Wei Yan[a], Yu Han[a], Ximing Qu[a], Shuhu Yin[a], Chi Chen[b], Ruiyin Ji[a], Yanrong Li[a], Guang Li[a], Gen Li[a], Yanxia Jiang[a]*, Shigang Sun[a]*

[a] State Key Laboratory of Physical Chemistry of Solid Surfaces,
Collaborative innovation center of Chemistry for Energy Materials,
Department of Chemistry, College of Chemistry and
Chemical Engineering, Xiamen University,
Xiamen 361005, People's Republic of China

[b]Shanghai Advanced Research Institute,
Chinese Academy of Sciences Shanghai,
201210, People's Republic of China

Correspondence to:

yxjiang@xmu.edu.cn, sgsun@xum.eudu.cn

Experimental Procedures

Supplementary Note 1 to 3
Supplementary Figures 1 to 37
Supplementary Tables 1 to 15
Supplementary References

Experimental Procedures

Methods

Synthesis of ZnCo-ZIF nanocube. The cube ZnCo-ZIF nanocrystals was synthesized according to a previous literature with some modifications[1, 2]. In a typical procedure, 2 mmol $Zn(NO_3)_2 \cdot 6H_2O$, 0.15 mmol $Co(NO_3)_2 \cdot 6H_2O$ and 10 mg cetyltrimethylammonium bromide (CTAB) were dissolved in 20 mL ultrapure water and then rapidly stirred to form a homogenous pick solution. In the meantime, 110 mmol 2-methylimidazole was dissolved in 140 mL ultrapure water. Subsequently, the pick solution was poured into the 2-methylimidazole solution and stirred for 12 h. Finally, the light purple precipitate was separated by centrifugation, and then washed thoroughly with ultrapure water for several times before drying at 60 °C in an oven for overnight.

Synthesis of *d*-(Co_{SA}-N-C) and Co_{NP}-N-C. For the synthesis of the *d*-(Co_{SA}-N-C), the ZnCo-ZIF@SiO_2 nanocube was first synthesized by the following steps: 500 mg of synthesized ZnCo-ZIF nanocube was dispersed in 240 mL ultrapure water, and then 6 mL of CTAB aqueous solution (25 mg mL^{-1}) and 10 mL of hydroxide sodium (NaOH) aqueous solution (6 mg mL^{-1}) were added to the above solution and stirred for 15 minutes. Tetraethyl orthosilicate (TEOS) (1.2 mL in 6 mL of methanol) was injected into the solution, and was stirred for different time (1, 3, 6 h) to synthesize ZnCo-ZIF@mSiO_2 with different silica thickness. The ZnCo-ZIF@mSiO_2 products were collected by centrifuging and then washed three times with ultrapure water and ethanol. The products were later dried at 60 °C in vacuum over overnight for subsequent use. In order to obtain *d*-(Co_{SA}-N-C), the as-prepared samples of ZnCo-ZIF@mSiO_2 were heated at 900 °C in a ceramic boat under Ar atmosphere for 2 h. After the products were cooled down to ambient temperature under the Ar flow, they were immersed in aqueous NaOH (2 M) solution. The *d*-(Co_{SA}-N-C) was collected by centrifugation and washed with ultrapure water and ethanol for several times and dried at 60 °C in vacuum over overnight. For comparison, a non-concave cubic control sample (Co_{NP}-N-C) was

synthesized using the same method as *d*-(Co_{SA}-N-C), but without SiO_2 coating.

Synthesis of *d*-(Co_{NP}/Co_{SA}-N-C). In order to obtain *d*-(Co_{NP}/Co_{SA}-N-C), 40 mg *d*-(Co_{SA}-N-C) and 4 mg Cobalt acetylacetonate were placed at the upstream side and the bottom of the porcelain boat, respectively. After rinsing with the Ar flow, the center of the furnace was raised to 180 °C at a heating rate of 2 °C min^{-1} and maintained at this temperature for 3 h. The temperature was further increased to 900 °C at a rate of 5 °C min^{-1}, held there for 3 h pyrolysis, and then cooled down to room temperature. As control samples, *d*-(Co_{NP}/Co_{SA}-N-C)-40:2, *d*-(Co_{NP}/Co_{SA}-N-C)-40:6 and *d*-(Co_{NP}/Co_{SA}-N-C)-40:8 samples were prepared in similar procedures.

Characterization. The overall particle size and distribution of the catalysts' morphologies were analyzed using scanning electron microscope (SEM, Hitachi s-4800) and transmission electron microscope (TEM, TECNAI F20). The images of single Co atoms were obtained by a high-angle annular dark-field scanning transmission electron microscopy (HAADF-STEM) on a Titan 80-300 scanning/transmission electron microscope operated at 300 kV, equipped with a probe spherical aberration corrector. The crystal phases present in each sample were identified using an automated Philips X'Pert Pro Super X-ray diffractometer (XRD) with Cu Kα radiation operating at 40 kV and 30 mA. X-ray photoelectron spectroscopy (XPS) measurements were performed on a PHI Quantun-2000 using Al Kα radiation (1846.6 eV) as the X-ray source. Inductively coupled plasma mass spectrometry (ICP-MS, Perkin Elmer Nexion 300) was applied to determine the concentration of Co elements in samples. X-ray absorption fine structure spectra (XAFS) at the Co K-edge were collected on the beamline BL14W1 in SSRF, provided by technical support of Ceshigo Research Service "www.ceshigo.com ". The radiation was monochromatized by a Si (111) double-crystal monochromator. The Co foil for Co K-edge was used to calibrate the energy, and the Co foil, CoPc and CoO were also tested for reference. The elemental distributions of Co, N and C were determined by energy-dispersive X-ray spectroscopy (EDS). Ultraviolet and visible spectra (UV-vis) were measured by a UV-2550

spectrophotometer. The surface area and micro/mesopore size distributions of the as-prepared materials were determined by the Brunauer-Emmett-Teller (BET) and Barrett-Joyner-Halenda (BJH) methods, respectively. Nitrogen adsorption-desorption isotherm tests were performed on a gas adsorption analyzer (Autosorb-iQ-XR).

Electrocatalytic Testing. All electrochemical measurements were conducted on a CHI 760e electrochemical workstation in a standard three-electrode system. The reference electrode was the saturated calomel electrode (SCE). A graphite rod was using as the counter electrode, and a glassy carbon electrode (GC) was using as the working electrode. Catalyst inks were prepared by ultrasonically dispersing 8 mg catalysts in 1 mL of solution containing 600 μL of isopropanol, 380 μL of ultrapure water and 20 μL of 5% Nafion solution. Then 25 μL catalysts ink was and dried to cover a rotating ring-disk electrode (RRDE, disk area: 0.2475 cm^2, Pt ring area: 0.1866 cm^2). In the end, the catalyst loading was about 0.8 mg cm^{-2} and 0.012 mg_{Pt} cm^{-2} for Pt/C. The potentials reported in this work were referred to reversible hydrogen electrode (RHE) by using the conversion equation:

$$E_{RHE} = E_{SCE} + 0.2415 + 0.059\ pH \quad (1)$$

In this work, the ORR polarization curves in linear sweep voltammetry (LSV) and cyclic voltammograms for all catalysts were obtained at a scan rate of 10 mV s^{-1} in O_2- or N_2-saturated 0.1 M $HClO_4$ solution. RRDE measurements were conducted by linear sweep voltammetry (LSV) with the potential range from 0.1 to 1.1 V at 900 rpm with a scan rate of 10 mV s^{-1}, while the ring electrode was held at 1.2 V. The number of electron transfer (n) and the % H_2O_2 were calculated by the following equations:

$$H_2O_2(\%) = 200\times(I_R/N)/(I_R/N+ I_D) \quad (2)$$

$$n = 4\ I_D/(I_R/N+ I_D) \quad (3)$$

where I_D is the disk current, I_R is the ring current, and N (0.37) is the current collection efficiency of the Pt ring. The electron transfer numbers of ORR were also determined from the slopes of the linear line according to the following K-L equation:

$$1/j = 1/j_k + 1/j_L = 1/j_k + 1/B\omega^{1/2} \quad (4)$$

$$B = 0.2nFC_0D_0^{2/3}V^{-1/6}H_2O_2(\%) = 200\times(I_R/N)/(I_R/N+ I_D) \quad (5)$$

where J is the measured current density, J_K is the kinetic current density, J_L is the diffusion-limited current density, ω is the electrode rotation rate, F is Faraday constant (96485 C mol^{-1}), C_0 is the bulk concentration of O_2 (1.2×10^{-3} mol L^{-1}), D_0 is the diffusion coefficient of O_2 (1.9×10^{-5} cm^2 s^{-1}) and ν is the kinetic viscosity of the electrolyte (0.01 cm^2 s^{-1}).

PEM fuel cell Testing. The MEAs for an H_2/O_2 PEM fuel cell were prepared using the hot-pressing method, reported previously by our group and conducted in a Model 850e fuel cell testing system (Scribner Associates, Inc.). In a typical approach, the test catalyst powder was dispersed in deionized water, and a Nafion solution (5 wt%) was directly deposited onto a gas diffusion layer (GDL, PTFE-pretreated Toray 060 carbon paper) in order to form the cathode catalyst layer. A commercial Pt/C catalyst was used at the anode. The active area of the MEA was 1.1 cm × 1.1 cm. The test catalyst loadings at the cathode were 4 mg /cm^2, and the Pt loadings at the anode was 0.4 mg/cm^2. The MEA was fabricated by hot-pressing the as-prepared cathode together with an anode, a Nafion membrane (NRE 211), and a gasket at 120 °C and 3 MPa for 2 min. The H_2 and O_2/air were fed as the fuel and oxidant with full humidification at 1/2 bar back pressure and a flow rate of 300 mL min^{-1} and 400 mL min^{-1}. The testing temperature of the fuel cell was 80 °C.

Theoretical calculations. All spin-polarized DFT calculations were performed using the Vienna ab initio Simulation Package (VASP)[3]. The PBE functional of the generalized gradient approximation was applied[4]. The kinetic cut-off energy of the planewave basis is 400 eV. The Van der Waals interaction was taken into account for all calculations[5]. During the geometry optimization, the energy and the force convergence criteria were 10^{-5} eV and 0.01 eV $Å^{-1}$. The dipole correction was performed when the convergence was achieved. The GGA+U method was applied to account for the strongly localized d orbitals of the Co atom of the CoN_4[6]. The Hubbard U values for the Co were chosen to be 3.1, 4.2, 4.9 and 5.3, respectively, attempting to have a brief insight into the intermediate adsorption at the Co atom during O_2 adsorption

and reduction. The computational hydrogen electrode (CHE) model was applied to calculate the free energy of reactions including a couple of electron and proton transfer. The entropy of H_2 in the gas phase was taken from the experimental value. The vacuum layer between the periodic images of the CoN_4 carbon sheets was 20 Å, and all atoms in the supercell were allowed to relax. For the geometry optimization, the Brillouin zone was sampled with a 6×6×1 k-point mesh of the Monkhorst–Pack scheme. In the NEB calculation, a 4x4x1 k-point mesh was applied instead. In order to study the crinkling structures, the carbon layer was extended and sampled with a 3×6×1 mesh for the crinkling structures H and D, respectively, and a 6×3×1 mesh for the structure P. In the NEB calculation, the force convergence was 0.05 eV $Å^{-1}$. The transition state was further searched by the dimer method and converged to the saddle point[7]. The free energy correction at room temperature was carried out by the numerical frequency computation, and the free energy was calculated according to $G=E-TS+\int C_p dT$.

Supplementary Note

Note 1

Metalorganic gaseous doping approach. Metalorganic gaseous doping strategy can significantly increase the density of active sites and effectively compensate for the loss of CoN_4 moieties on the external porous carbon layer caused by the etching of silica layer. First, we conduct a thermogravimetric test on the $Co(acac)_3$ to determine the evaporation temperature. Under this temperature, the solid $Co(acac)_3$ is slowly evaporated into the catalyst phase in the form of gaseous molecules, and the size of O_2 molecule is smaller than that of the $Co(acac)_3$ molecule. Theoretically, the position where $Co(acac)_3$ molecule can reach can also be reached by O_2 molecule, which greatly improves the utilization of active sites.

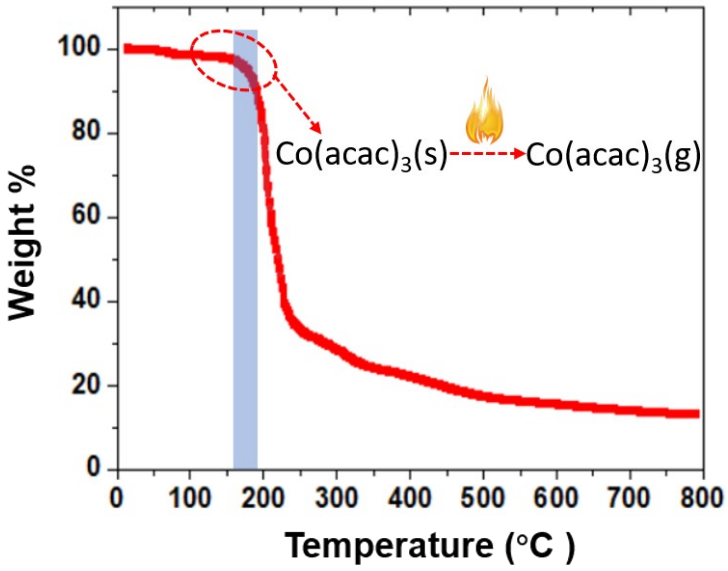

TGA curve of $Co(acac)_3$ under nitrogen with a heating rate of 10 °C min^{-1}.

Note 2

Theoretical study. For O_2 adsorption at the Co_4-CoN_4 structure, there were the side-on and the end-on configurations at the high spin Co center. In addition, there was the end-on configuration at the low spin state, which was less stable than the same

configuration at the high spin state, as shown in **Table S10**. Another structure was considered that the Co cluster located on the carbon layer near the CoN_4 moiety, i.e. $Co_4(C_g)$-CoN_4. Different O_2 adsorption configurations were studied as shown in **Table S11**. Based on the Bader population analysis, the partial charges of the O atoms are listed in **Table S12**. The high spin state of the Co_4-CoN_4 corresponded to more negative partial charges of the O atoms than the other CoN_4 structures. This can agree with the trends the O_2 adsorption energy and the O-O bond length at the relevant structures.

Analogous to O_2 adsorption, the Co_4-CoN_4 can enhance OOH adsorption and weaken the O-O bond more than the other structures. It was found out the relevant dissociation pathway in the M2 can include the M1 as the first step, implying a strong OH adsorption at the Co center of the Co_4-CoN_4. Therefore, the barrier in the M1 was considered for the OOH dissociation at the Co_4-CoN_4. The ORR free energy at the CoN_4 and the Co_4-CoN_4 were compared at 0.85 V, as shown in Supplementary **Figure 29**. It was found out that H_2O_2 can be formed at the CoN_4, although its formation is more endothermal than other possible intermediates at the CoN_4. This agree with the experimental phenomena that H_2O_2 is a side-product during ORR at the CoN_4. Whereas, the H_2O_2 formation cannot exist at the Co_4-CoN_4. In addition, the OOH dissociation can be favored at the Co_4-CoN_4 as shown in **Table S15**. These were also consistent with the experimental findings that H_2O_2 yield was significantly low at the *d*-(Co_{NP}/Co_{SA}-N-C) catalyst. Moreover, the OH and O intermediates can be strongly adsorbed at the Co center of the Co_4-CoN_4 rather than the CoN_4. The intermediate structures such as *OH*OH and *O*OH became more stable at the Co_4-CoN_4 rather than the CoN_4. These radicals were very reactive in the ORR potential range. Their desorption from the Co center can be weakened rather than the CoN_4.

Therefore, the overall ORR activity can be maintained and the side reaction about radicals attacking the carbon layer can be alleviated significantly. The catalyst performances on the ORR reactivity and durability can be improved at the *d*-(Co_{NP}/Co_{SA}-N-C) catalyst.

Moreover, the free energy of the intermediate in the most stable structure has been chosen to plot the free energy profile. The potential correction has been carried out at

0.85 V to have a comparison between the CoN_4 and the Co_4-CoN_4 structures on ORR, which can provide insights into the ORR reactivity toward a certain intermediate as well as intermediate adsorption caused by the incorporation of the Co nanoparticle. Although the thermodynamic limiting potential at which all the reactions steps are downhill in free energy can be applied to calculate the theoretical overpotential, it shall be noted that this theoretical overpotential cannot be compared directly with a measured overpotential in experiment, which depends on the current density[8]. Moreover, the Co_4-CoN_4 in the theoretical study can be a conceptual structure related to a unique kind of the active site in the real catalyst. Therefore, there is no intension to find out the thermodynamic limiting potential in comparison with experiment.

The outer layers of the catalyst were curved and distorted to a certain extent, so there can be some CoN_4 active sites in deformed geometries. In order to understand O_2 activation at these deformed active sites, the basic cases that the CoN_4 structure was crinkled along different axes respectively were studied. In the deformed geometries crinkling along the H axis, the distance between the C atoms in the two pentagonal rings (L_{cp}) was decreased along the crinkling, whereas the distance between the C atoms in the two hexagonal rings (L_{ch}) changed barely, as shown in **Figure S30**. These can imply that the carbon matrix structure around the CoN_4 moiety can be maintained along the axis direction during the gradual crinkling and cannot be influenced by the change in the CoN_4 geometry. The same trend was found out in the deformed geometries along the P axis, as shown in **Figure S34**. When the CoN_4 structure was distorted along the D axis, it can lead to the crinkling along the H and the P axes to some extent at the same time. Therefore, the tendencies of the L_{ch} and the L_{nh} variations can be superposed together and the L_{ch} was increased as a function of the L_{cp}. The CoN_4 crinkling along the H and the D axis can generally result in the high spin Co center and enhance O_2 activation rather than the planar CoN_4 structure. The distances L_{np} and L_{nh} can vary in the same trend in the H and the D structures. Moreover, the high spin Co center was closely related to O_2 activation in these deformed structures. However, for the deformed P structures, the L_{np} and the L_{nh} changed in contrary trends to those in the H structures and the low spin Co center was dominant along the gradual crinkling. Corresponding,

the P structures showed a weak effect on O_2 activation. The CoN_4 crinkling can cause the change in the electronic structures of the C atoms around by the CoN_4 geometry. When the CoN_4 geometry was crinkled along the H axis, for instance, the nearby three C atoms in the hexagonal ring can transform to trigonal pyramidal shape as indicated in **Figure S30**. This can imply that the sp^2 hybridization of the three C atoms was converted partially to the sp^3 hybridization. Analogously, it can take place for the two C atoms in the pentagonal ring when the CoN_4 geometry was crinkled along the P axis. This partial conversion can be hindered considerably more between the two C atoms in the pentagonal ring than between the three C atoms in the hexagonal ring, due to the local conformation difference in those structures. Therefore, these could lead to different trends on the CoN_4 geometry variations as shown in **Figure S31, S33 and S34.** The high spin Co center can be favored at the H and the D structures with an effect on O_2 activation.

OOH adsorption was enhanced at the H and the D structures along the CoN_4 crinkling, respectively, as shown in **Figure S35**. The corresponding O-O bond length was elongated more noticeable in the D structures. OOH adsorption at the P structure was enhanced when the deformed CoN_4 structure was folded in a certain extent. The crinkling extent effect on the ORR intermediates adsorptions was studied at the H_b and H_c structures, as shown in **Figure S36**. Compared with the planar CoN_4, it can be found out that O and OH adsorptions at the Co center were significantly enhanced at the two deformed structures. The intermediates such as *O*OH and *OH*OH were also favored more than at the planar CoN_4, and their energy differences to the stable intermediates became gradually smaller as the crinkling extent was increased. However, H_2O_2 adsorption was not influenced in a limited extent along the crinkling extent. These can suggest that the chemical desorption of radicals from the active site can be weakened significantly. Therefore, those deformed CoN_4 sites can somewhat diminish the side reaction about the radicals attacking the carbon layer as discussed at the Co_{NP}-CoN_4 composite site, resulting in the improved performances of both reactivity and durability at the catalyst.

The active sites of deformed geometries in the outer layers were mainly related to the CoN_4 structure. The Co_{NP}-CoN_4 composite site in deformed geometry could coexist with the site in planar structure inside the catalyst. Compared with the deformed CoN_4 structure, the deformed Co_4-CoN_4 composite site can enhance O_2 activation, as shown in **Figure S37**. For instance, there was a very weak O_2 activation at the P_a structure, whereas O_2 adsorption energy became more negative and the O-O bond can be elongated significantly after the incorporation of the Co_4 cluster into the P_a structure. This can suggest that O_2 dissociation can be facilitated and a four-electron pathway can be favored as discussed at the normal Co_4-CoN_4 structure. In addition, there was no intention to compare O_2 activation effects between the deformed and the normal Co_4-CoN_4 structures, due to the complicatedness of the structural variety that was beyond the scope in this work.

Note 3

PEM fuel cell durability. In the electrochemical measurement (i.e. the RDE measurement), a simple solid-liquid interface with an efficient mass transport can be maintained well during the ORR. The durability decay in a long run of electrochemical measurement can be ascribed to a slight dissolution of active site. The performance degradation in the fuel cell is complicated and elusive to study. To our best knowledge, there are several issues in general, such as (1) the demetallation of active sites, (2) the electrochemical oxidation of carbon skeleton at relatively high voltage, (3) the attack on carbon skeleton and active sites by H_2O_2/radicals, and (4) the micropore blockage by flooding, which can be proposed as the primary mechanisms for the performance degradation in the fuel cell[9, 10]. Those can result in the TPB decomposition and also the low TPB efficiency on ORR.

In the fuel cell, the TPB structure can be very irregular and the mass transport to the TPB can significantly influence the ORR activity, given that the catalyst component can be stable enough in the fuel cell. When the catalyst shows a better ORR activity at a high potential, its fuel cell performance can suffer more dramatically from the mass transport at a relatively high output voltage. In general, the mass transport to the TPB

can depend on several factors, such as the catalyst mesoporosity, the preparation membrane-electrode assembly (MEA) and the micropore blockage by flooding. Since the SiO_2 coating procedure can bring out a better mesoporosity of the catalyst, e.g. *d*-(Co_{NP}/Co_{SA}-N-C) and *d*-(Co_{SA}-N-C), the MEA preparation and the micropore blockage could be the main reasons resulting in the current density decay in the fuel cell of this work. The MEA needs to maintain enough pore networks for gas diffusion. In addition, the micropore blockage by flooding can usually take place in the MEA, whereas it can be ignored in the RDE measurement. The gaseous O_2 shows a very low solubility in water at the fuel cell operation condition compared with the electrochemical measurement. When a large amount of water from the ORR cannot be released in time, the O_2 diffusion to the active site of the TPB can be inhibited to some extent. The carbon-based catalyst usually works with an enough high loading. This requires a thick catalyst layer, which can cause a high resistance to the mass transport. When the pore networks are not homogeneously distributed in the MEA, the micropore blockage can evolve very severely as the fuel cell runs in a long period. The gradual loss of the TPB for ORR contributes to the overall durability performance decaying along the fuel cell test. In addition, the catalyst stability can be an important issue in the fuel cell. Owing to the electrochemical or chemical side reactions related to the radical oxygen species and H_2O_2, it is inevitable that the decomposition of carbon skeleton and the dissolution of active site can happen during the ORR in acid. Therefore, the non-precious metal cathode catalyst can suffer more than the Pt-group catalyst in the fuel cell. It should be noted that the mass transport is in a perfect condition in the electrochemical measurement and the catalyst loading is much lower than in the fuel cell test. Therefore, the radicals that are once generated can be transferred immediately to the composite site, which can show a strong tendency to bond the radical rather than the CoN_4 site, for a further ORR reaction in electrochemical measurement. We can propose that the kinetic aspect of the ORR at the catalyst can still work in the MEA as in the RDE measurement. However, the slow mass transport in the fuel cell can lead to a significant accumulation of the ROS and H_2O_2 in the MEA, which is detrimental to the catalyst stability. This degradation tendency can be intensified at the very thick catalyst layer.

The Co_{NP}-N-C showed a low ORR reactivity (i.e. a relatively high selectivity to H_2O_2 formation) and a poor mesoporosity. In the fuel cell tests, correspondingly, we found out that the MEA with the Co_{NP}-N-C degraded very fast (i.e. 75% current density loss within 20h), showing the worst durability among the three catalysts. The *d*-(Co_{NP}/Co_{SA}-N-C) and the *d*-(Co_{SA}-N-C) can show a better mesoporosity, so that the TPB can be constructed massively to favor the mass transport. Correspondingly, the carbon skeleton decomposition and the active site dissolution can be alleviated to some extent. As shown in **Figure 5f and Figure S27c**, their current densities at the beginning of the test can be ranked in a sequence as *d*-(Co_{NP}/Co_{SA}-N-C) > *d*-(Co_{SA}-N-C) > Co_{NP}-N-C. After 100h operation, the *d*-(Co_{NP}/Co_{SA}-N-C) can maintain about 48.6% of the maximum current density, showing a better durability than the *d*-(Co_{SA}-N-C) (about 44%). The current densities decayed in similar patterns between the *d*-(Co_{NP}/Co_{SA}-N-C) and the *d*-(Co_{SA}-N-C) during the tests. Those catalysts were synthesized by the same SiO_2 coating procedure with an equivalent mesoporosity. Therefore, we can suggest that the fuel cell performance degradation of those catalysts could take place in a similar mechanism related to the mass transport. In the electrochemical measurement, the Co_{NP} was found out to show a good electrochemical stability in the *d*-(Co_{NP}/Co_{SA}-N-C). It can be proposed that the Co_{NP} can also be stable enough within 100h operation in the fuel cell test. Otherwise, it would be estimated that the two current density plots in Fig. 2f can intersect if the Co_{NP} can dissolve very fast. The comparisons of the fuel cell tests among the three catalysts can help to explain the importance of the Co_{NP} in maintaining the activity and the durability of the catalyst during the ORR. Considering the intricacy of the MEA structure in a microscale, the study of improving the mass transport in the MEA is not the interest of in this work currently. The relevant study will be a focus of our work in the future.

Supplementary Figures

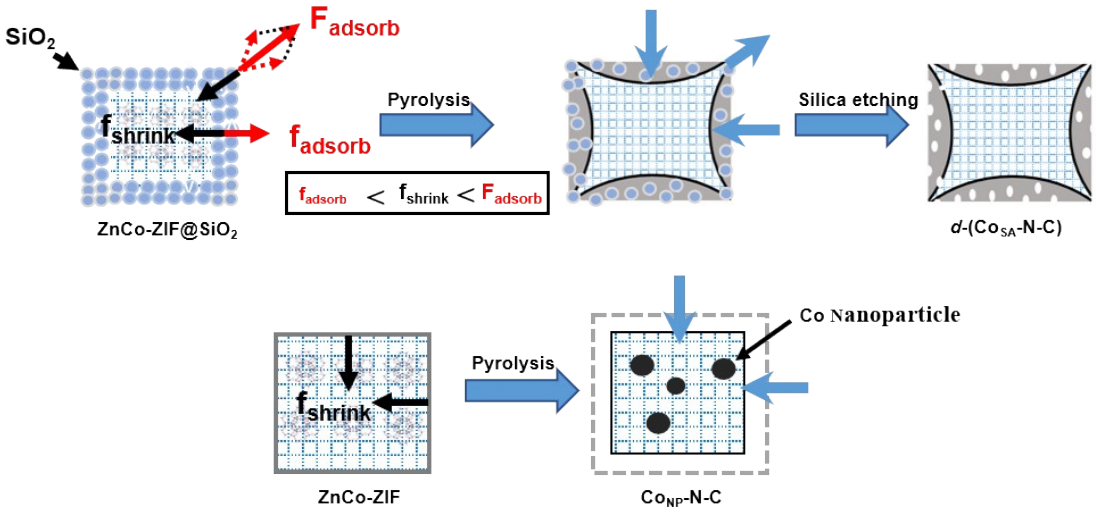

Figure S1. Schematic illustration of the synthesis process of *d*-(Co_{SA}-N-C) and Co_{NP}-N-C.

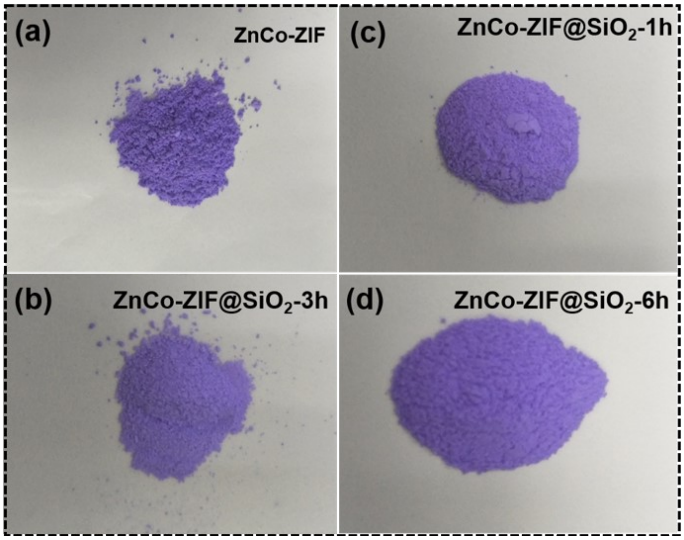

Figure S2. Optical photographs of (a) Zn,Co-ZIF, (b) ZnCo-ZIF@mSiO_2-1h, (c) ZnCo-ZIF@mSiO_2-3h and (d) ZnCo-ZIF@mSiO_2-6h.

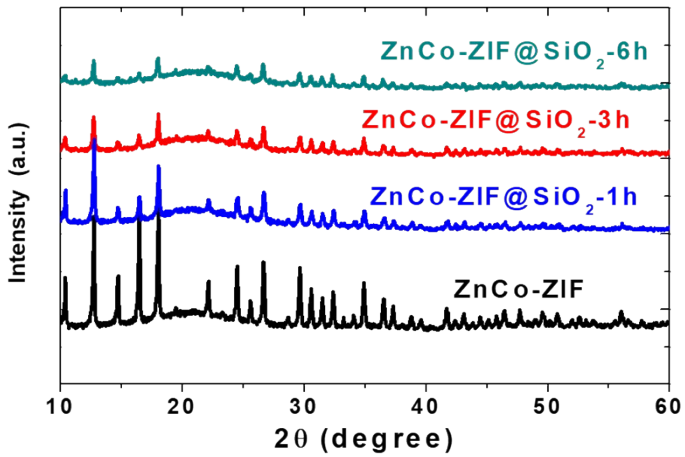

Figure S3. PXRD patterns of Zn,Co-ZIF, ZnCo-ZIF@mSiO$_2$-1h, ZnCo-ZIF@mSiO$_2$-3h and ZnCo-ZIF@mSiO$_2$-6h.

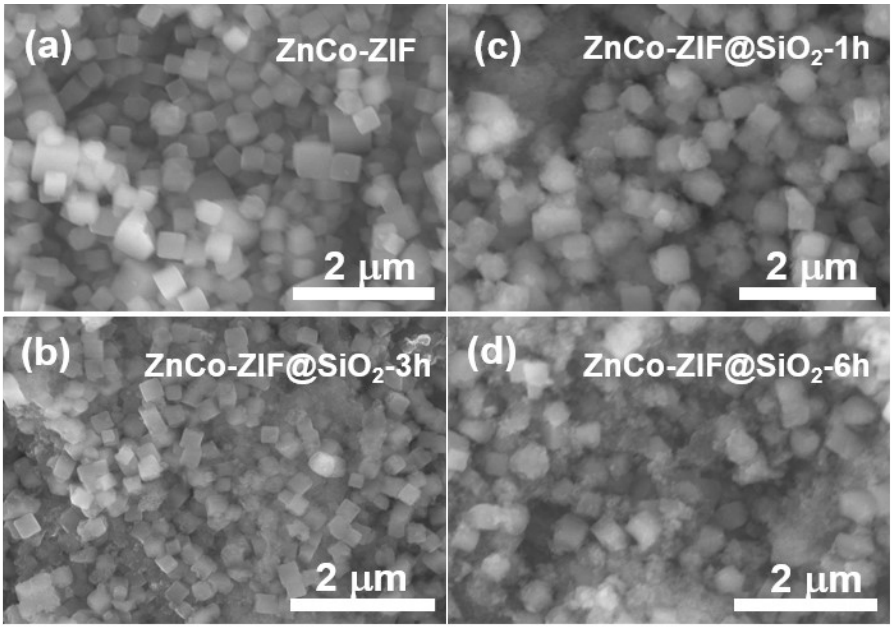

Figure S4. SEM images of (a) Zn,Co-ZIF, (b) ZnCo-ZIF@mSiO$_2$-1h, (c) ZnCo-ZIF@mSiO$_2$-3h and (d) ZnCo-ZIF@mSiO$_2$-6h.

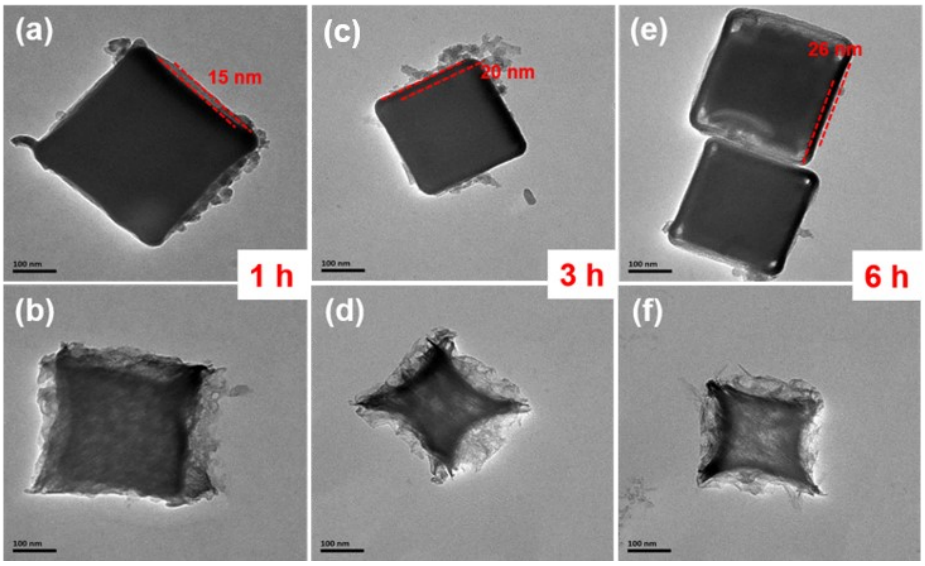

Figure S5. The Effect of silica coating thickness on catalyst morphology. TEM images of *d*-(Co_{SA}-N-C) made with different silica coating thickness: (a,b) 1h, 15 nm; (c,d) 3h, 20 nm; (e,f) 6h, 26 nm.

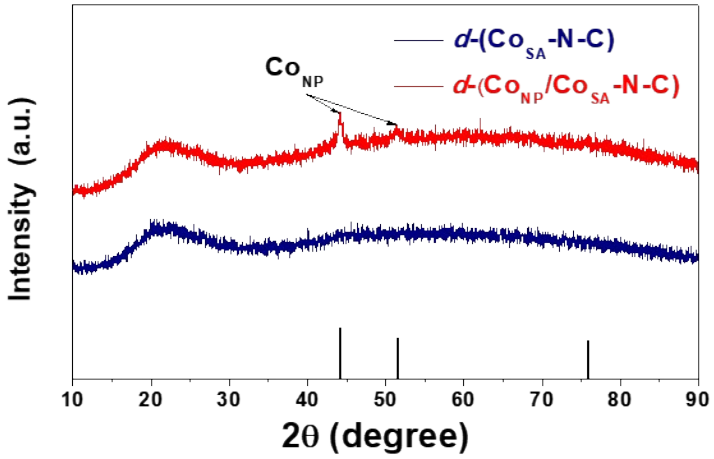

Figure S6. PXRD patterns of *d*-(Co_{SA}-N-C) and *d*-(Co_{NP}/Co_{SA}-N-C).

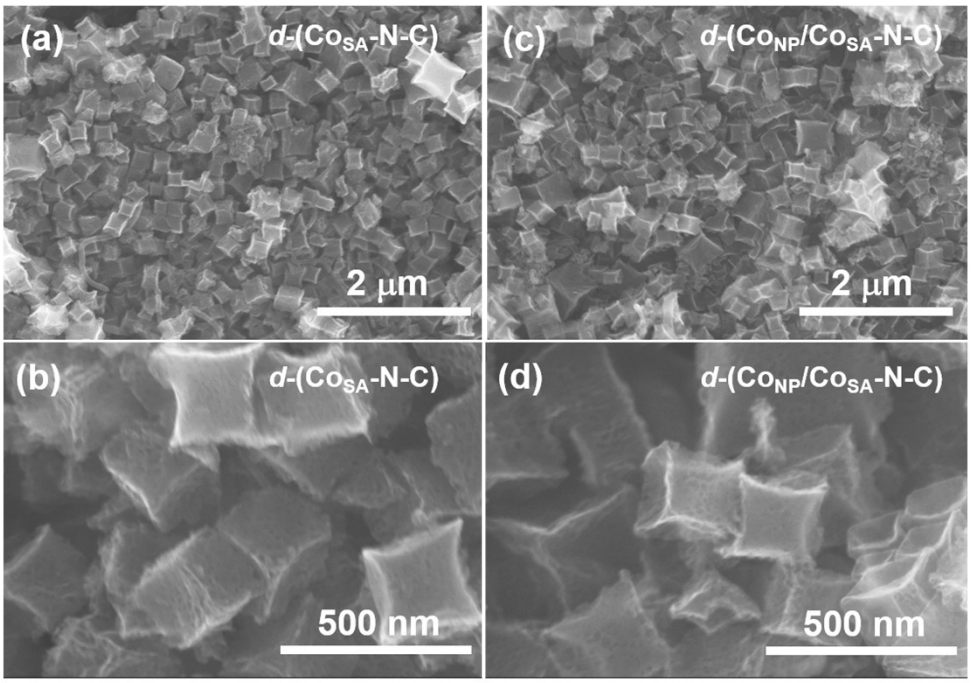

Figure S7. SEM images of (a,b) *d*-(Co$_{SA}$-N-C), (c,d) *d*-(Co$_{NP}$/Co$_{SA}$-N-C).

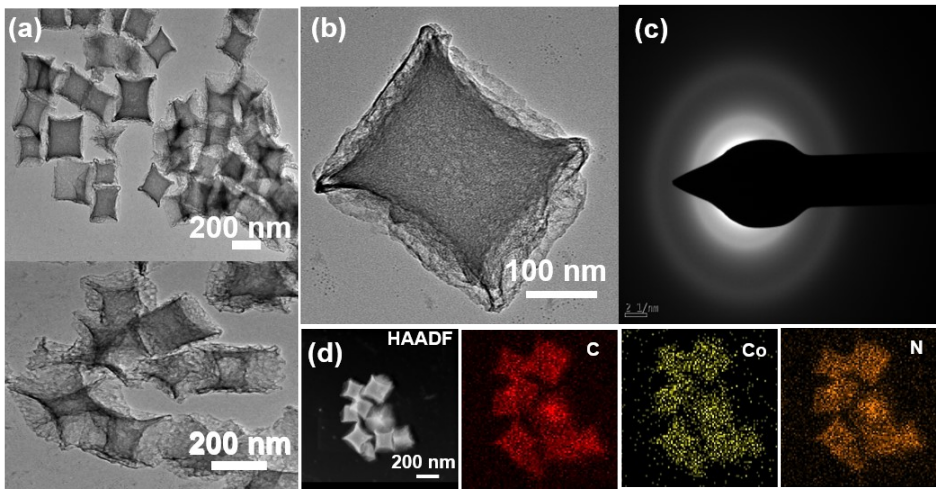

Figure S8. (a,b) TEM image and (c) corresponding SAED pattern of *d*-(Co$_{SA}$-N-C), (d) HADDF STEM image of *d*-(Co$_{SA}$-N-C) and corresponding element mapping.

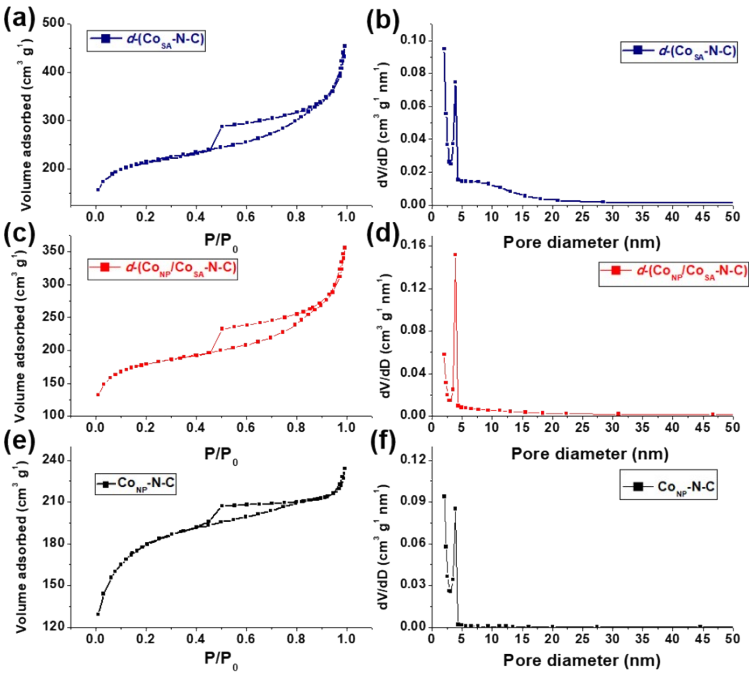

Figure S9. (a,c,e) N_2 sorption isotherms of *d*-(Co_{SA}-N-C), *d*-(Co_{NP}/Co_{SA}-N-C) and Co_{NP}-N-C, respectively. (b,d,f) pore size distributions of *d*-(Co_{SA}-N-C), *d*-(Co_{NP}/Co_{SA}-N-C) and Co_{NP}-N-C, respectively.

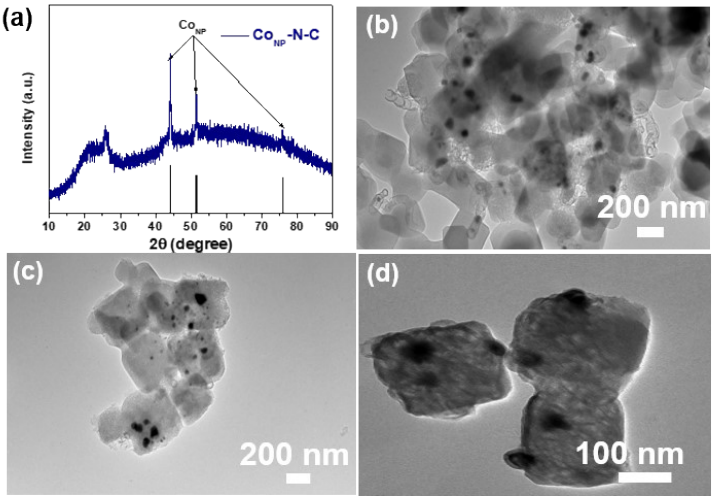

Figure S10. (a) XRD pattern of Co_{NP}-N-C, (b-d) TEM image of Co_{NP}-N-C. There were some peak corresponding to the metallic Co phase and a severe aggregation of Co nanoparticles up to 40 nm in diameter inside the catalyst, indicating the SiO_2-assisted MOF pyrolysis strategy can effectively improve the dispersion of metal active sites and tailor the microstructure.

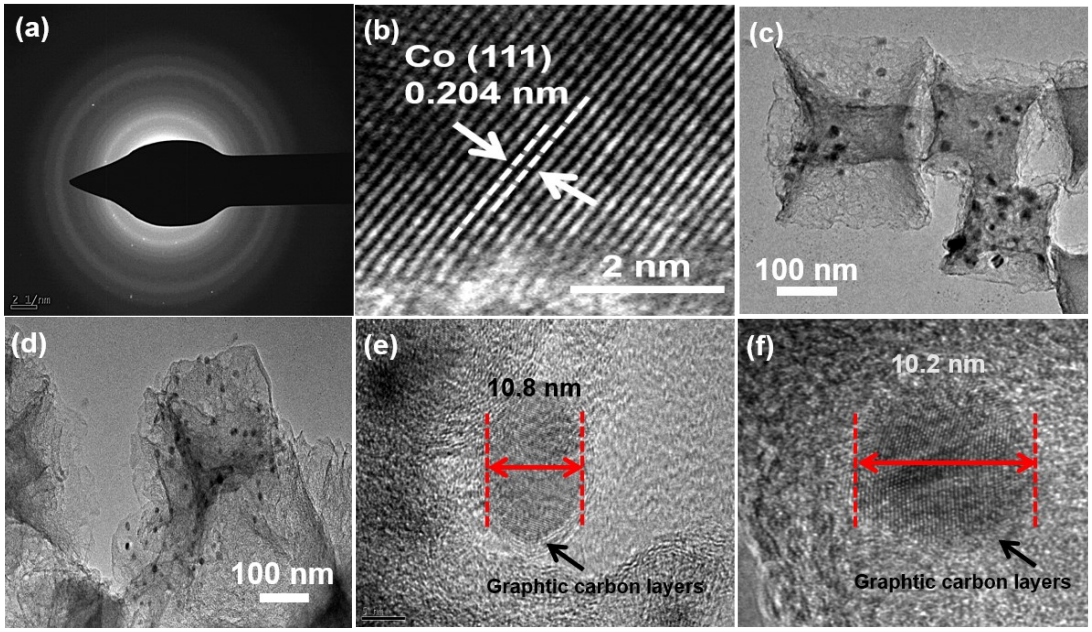

Figure S11. (a) corresponding SAED pattern of *d*-(Co_{NP}/Co_{SA}-N-C), (b) High-resolution transmission electron microscopy image of *d*-(Co_{NP}/Co_{SA}-N-C) nanoparticles, (c-f) TEM image shows the distribution and size of Co nanoparticles (Co_{NP} are wrapped in different layers of graphene).

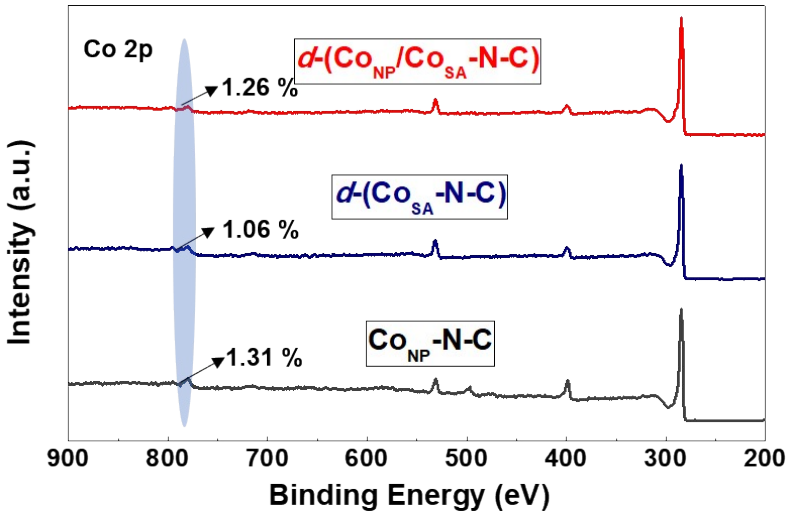

Figure S12. XPS survey spectra of Co_{NP}-N-C, *d*-(Co_{SA}-N-C), *d*-(Co_{NP}/Co_{SA}-N-C).

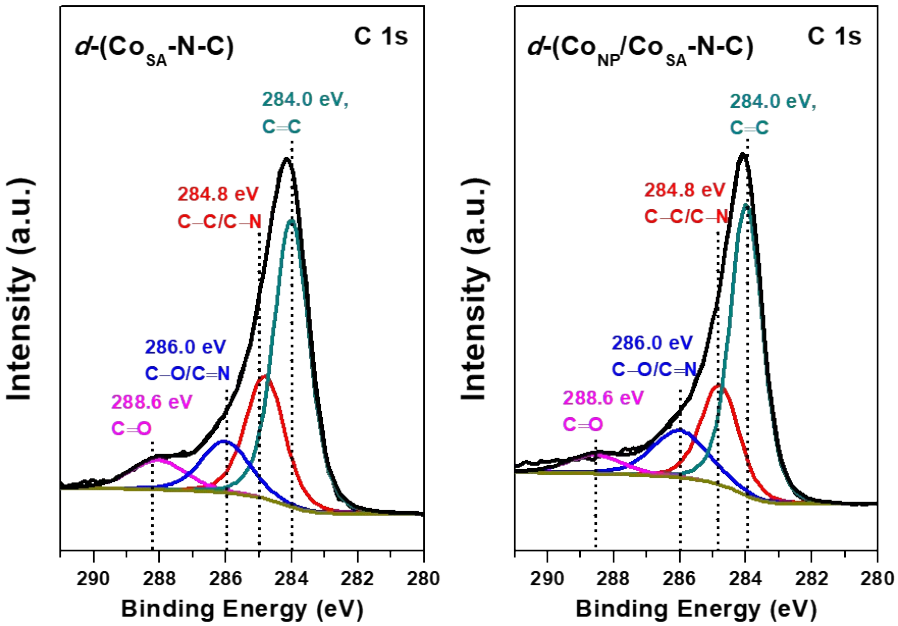

Figure S13. XPS C 1s analysis of the *d*-(Co_{SA}-N-C), and the *d*-(Co_{NP}/Co_{SA}-N-C) catalysts.

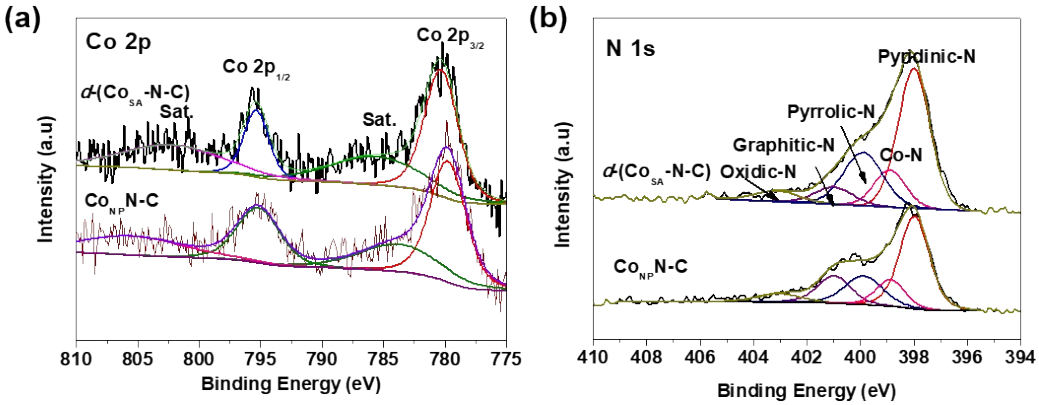

Figure S14. XPS Co 2p analysis of the (a) *d*-(Co_{SA}-N-C), Co_{NP}-N-C catalysts and (b) N 1s analysis of the *d*-(Co_{SA}-N-C), and the Co_{NP}-N-C catalysts.

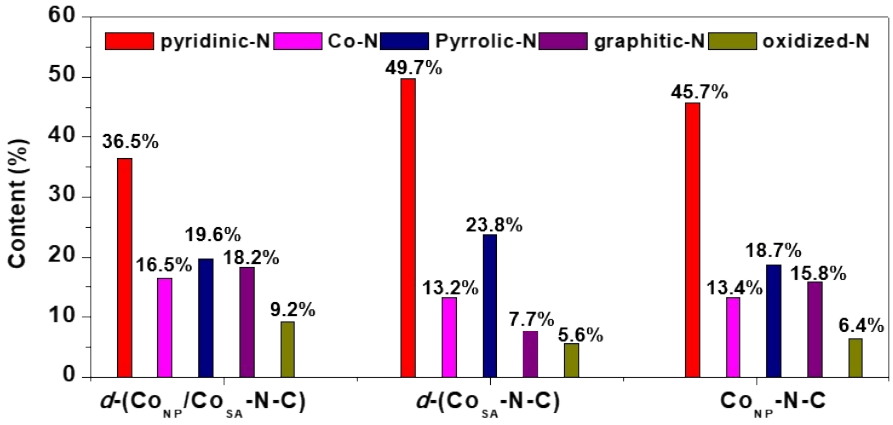

Figure S15. Relative content of various N species in the catalysts: *d*-(Co_{NP}/Co_{SA}-N-C), *d*-(Co_{SA}-N-C), and the Co_{NP}-N-C catalysts.

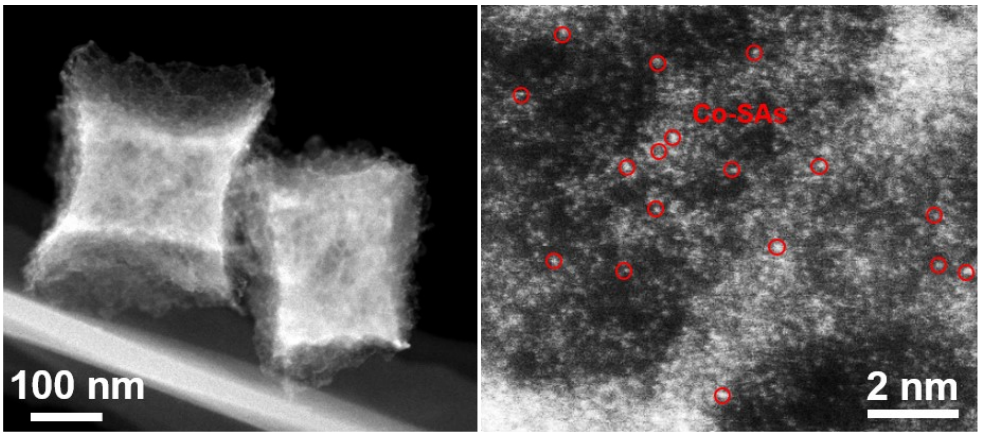

Figure S16. The aberration-corrected HAADF-STEM images and the enlarged images of the *d*-(Co_{SA}-N-C) catalyst. Bright spots represent the uniformly and densely distributed Co single-atoms. Some are highlighted by red circles.

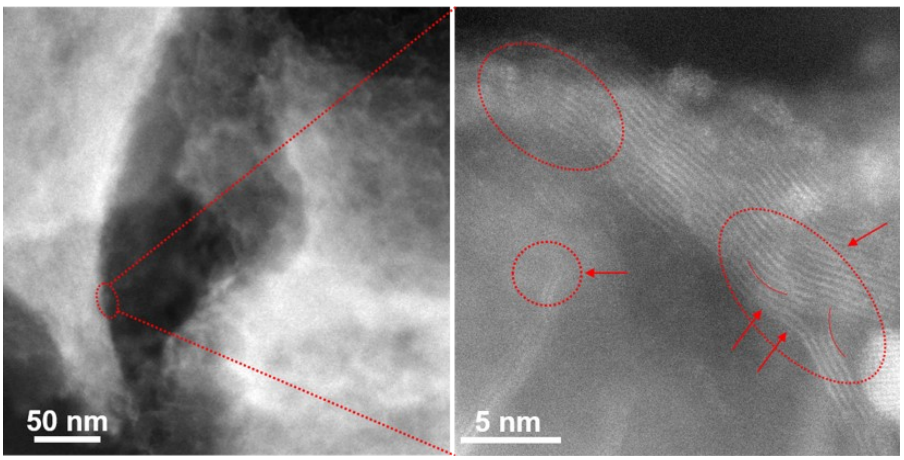

Figure S17. The aberration-corrected HAADF-STEM images and the enlarged images of the *d*-(Co_{SA}-N-C) catalyst. Some carbon lattice deformities are highlighted by red circles.

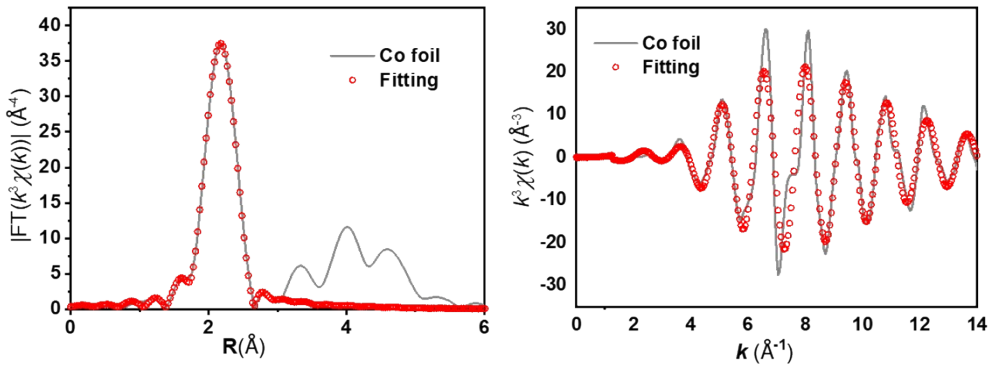

Figure S18. EXAFS fitting curves of Co foil. (a) EXAFS R space fitting curves for the Co-Co shell and (b) EXAFS k space signal from the first Co-Co shell of Co foil.

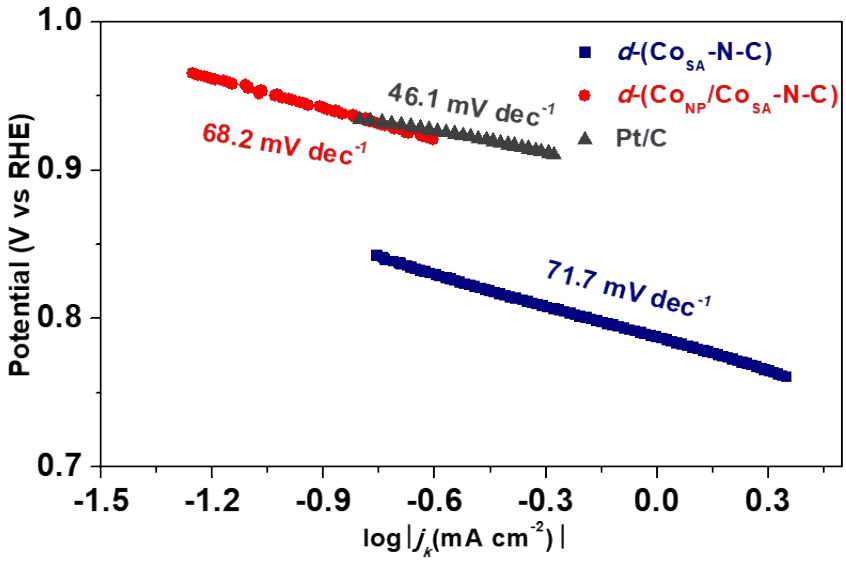

Figure S19. Tafel plots curves of *d*-(Co_{SA}-N-C), *d*-(Co_{NP}/Co_{SA}-N-C), and Pt/C, respectively. display Tafel slopes of 71.7, 68.2 mV and 46.1 mV decade^{-1}, respectively.

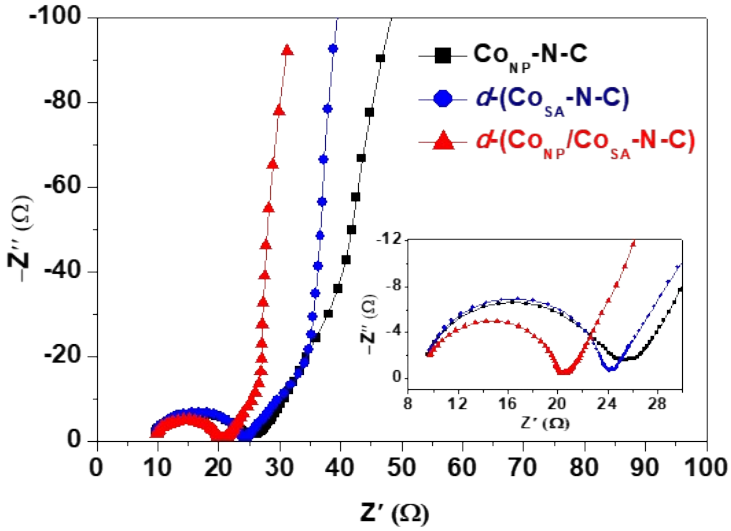

Figure 20. EIS spectra of Co_{NP}-N-C), *d*-(Co_{SA}-N-C) and *d*-(Co_{NP}/Co_{SA}-N-C). Inset is a local enlargement.

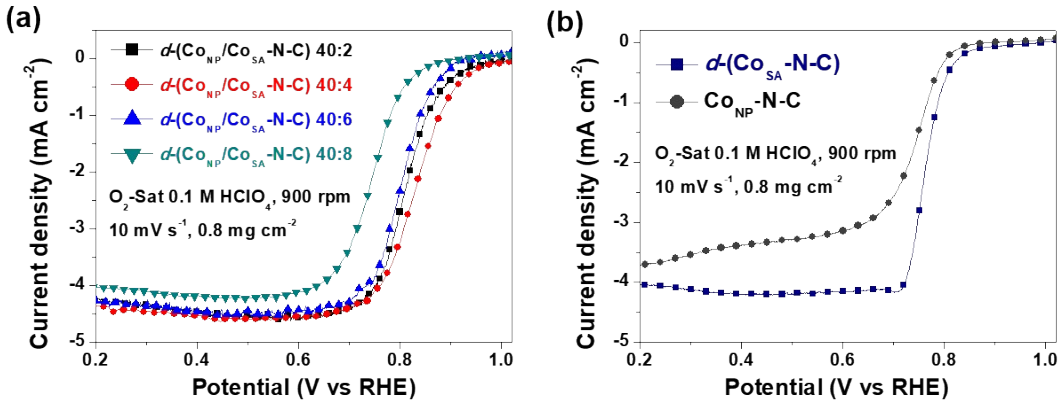

Figure S21. (a) The effect of *d*-(Co_{SA}-N-C)/$Co(acac)_3$ ratios on the ORR activity of the *d*-(Co_{NP}/Co_{SA}-N-C) catalyst and (b) the silica coating on the ORR activity of the *d*-(Co_{SA}-N-C).

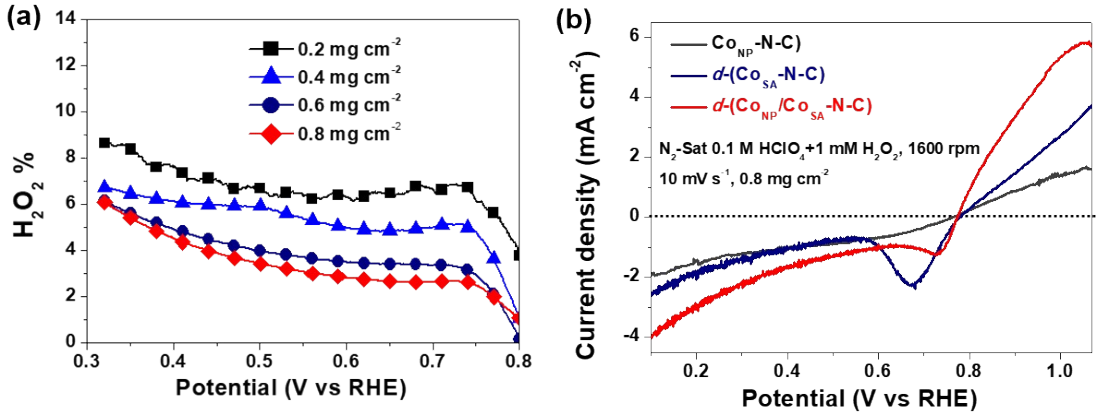

Figure S22. (a) The loading dependence of H_2O_2 yields of the *d*-(Co_{NP}/Co_{SA}-N-C) catalyst during the RRDE tests. When catalyst loadings vary at a wide range from 0.2 to 0.8 mg/cm^2, H_2O_2 yields remain at a very low level. This can further suggest that the 4e- ORR can be dominant on *d*-(Co_{NP}/Co_{SA}-N-C) catalyst, rather than the 2e-+2e- pathway. (b) H_2O_2 reduction of the Co_{NP} -N-C, *d*-(Co_{SA}-N-C) and *d*-(Co_{NP}/Co_{SA}-N-C) catalysts in N_2-saturated 0.1M $HClO_4$ and 1 mM H_2O_2. H_2O_2 reduction starts around 0.78 V, above which H_2O_2 oxidation to O_2 can happen. The Co_{NP}-N-C shows a weaker interaction with H_2O_2 than the other two catalysts, so its oxidation current is lower and there is not clearly a reductive peak in the negative-going scan. This peak can be partially related to the reduction of molecular O_2 generated by H_2O_2 oxidation. The active sites of the *d*-(Co_{NP}/Co_{SA}-N-C) and the *d*-(Co_{SA}-N-C) can enhance O_2 dissociation in different extents, so that ORR can take place via the 2e-+2e- pathway at the *d*-(Co_{SA}-N-C) relatively more than at the *d*-(Co_{NP}/Co_{SA}-N-C). In a potential range below 0.6 V, it is clear that H_2O_2 reduction can prevail at the *d*-(Co_{NP}/Co_{SA}-N-C) rather than the other catalysts. This can suggest that the Co_{NP}-CoN_4 composite site can enhance H_2O_2 conversion, which can help to maintain the activity and the durability in the electrochemical measurement.

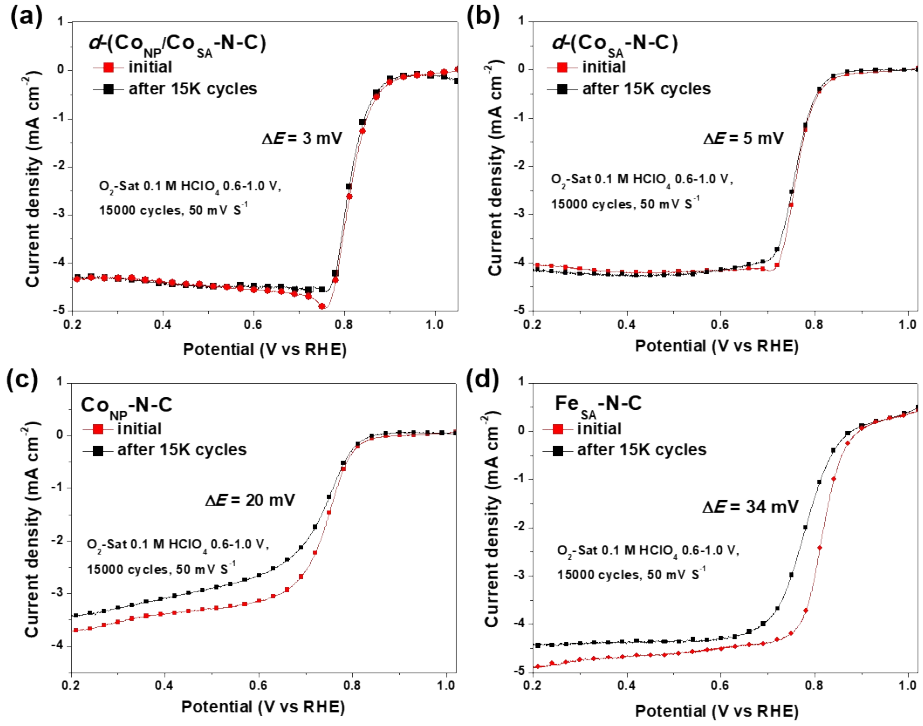

Figure S23. The ORR polarization curves of (a) *d*-(Co_{NP}/Co_{SA}-N-C), (b) *d*-(Co_{SA}-N-C), (c) Co_{NP}-N-C and Fe_{SA}-N-C before, and after 15K cycles between 0.6 and 1.0 V versus RHE in 0.1 M $HClO_4$. As control sample, the Fe_{SA}-N-C sample was synthesized using the same method as Co_{NP}-N-C, but $Fe(NO_3)_3.9H_2O$ instead of $Co(NO_3)_2.6H_2O$.

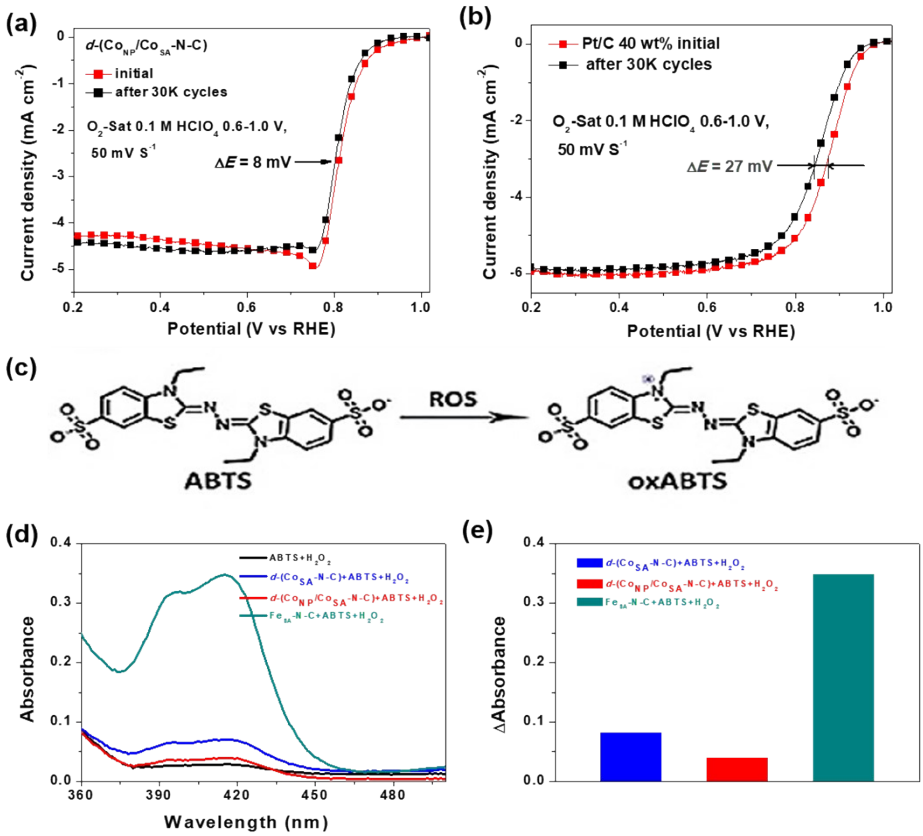

Figure S24. The ORR polarization curves of (a) *d*-(Co_{NP}/Co_{SA}-N-C) and (b) Pt/C before and after 30K cycles between 0.6 and 1.0 V versus RHE in 0.1 M $HClO_4$. (c) Reaction between ROS and ABTS. (d) UV-vis absorption spectra of 0.1 M $HClO_4$ include ABTS and H_2O_2; *d*-(Co_{SA}-N-C), ABTS and H_2O_2; *d*-(Co_{NP}/Co_{SA}-N-C), ABTS and H_2O_2; Fe_{SA}-N-C, ABTS and H_2O_2. (e) presents the absorbance change at 417 nm after subtraction of the value of ABTS + H_2O_2 treated solution.

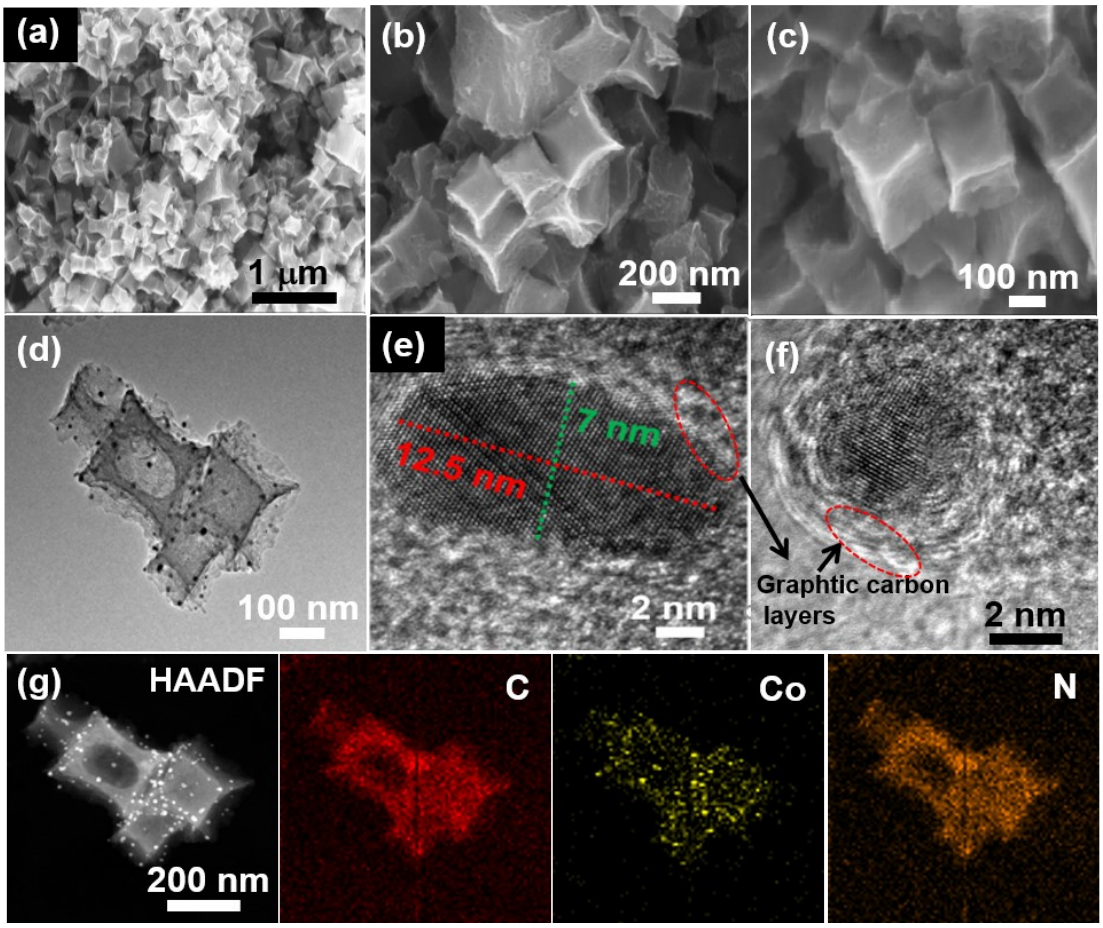

Figure S25. The SEM image (a-c), TEM image (d-f) and (g) Elemental mapping images of *d*-(Co_{NP}/Co_{SA}-N-C) obtained after 50K cycles of RDE tests.

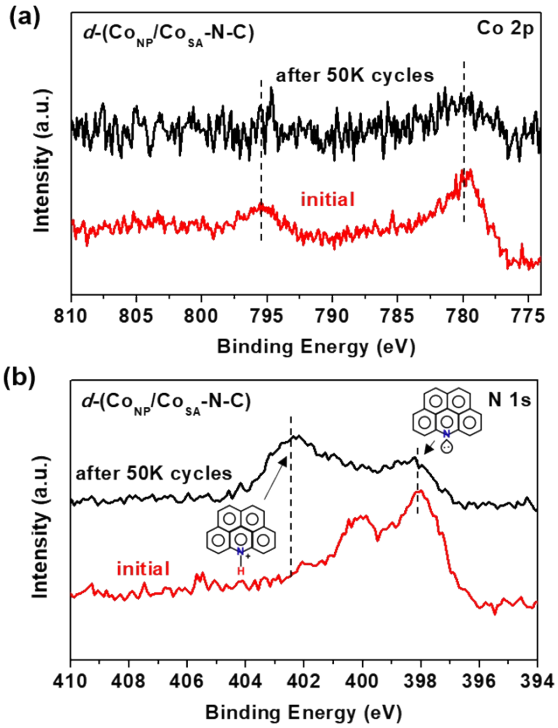

Figure S26. The comparison of Co 2p (a) and N 1s (b) XPS of *d*-(Co_{NP}/Co_{SA}-N-C) obtained after 50K cycles of RDE.

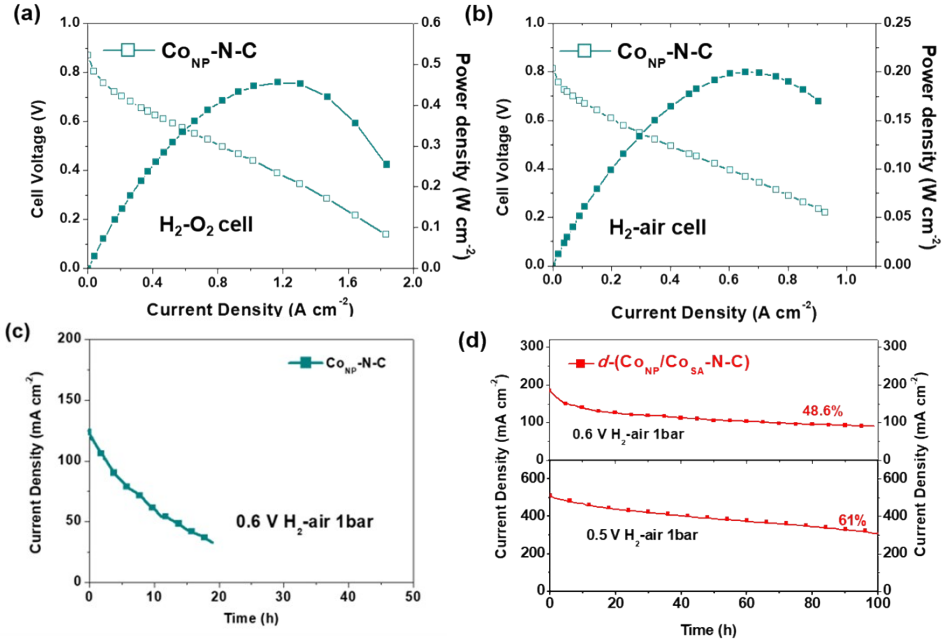

Figure S27. (a) H_2-O_2, (b) H_2-air MEA performance of Co_{NP}-N-C cathode. (c) Durability tests of the Co_{NP} -N-C catalyst in MEA in 1 bar H_2/air at a constant cell voltage of 0.6 V for 20 h. (d) Comparison of the durability test of the *d*-(Co_{NP}/Co_{SA}-N-C) catalyst in MEA in 1 bar H_2/air at a constant cell voltage of 0.5/0.6 V for 100 h. Other parameters: cathode ≈4.0 mg cm^{-2}, anode ≈0.4 mg_{Pt} cm^{-2} Pt/C, O_2 400 slpm and H_2 300 slpm, 100% RH, cell 80 °C, membrane Nafion 211, MEA active area: 1.21 cm^2.

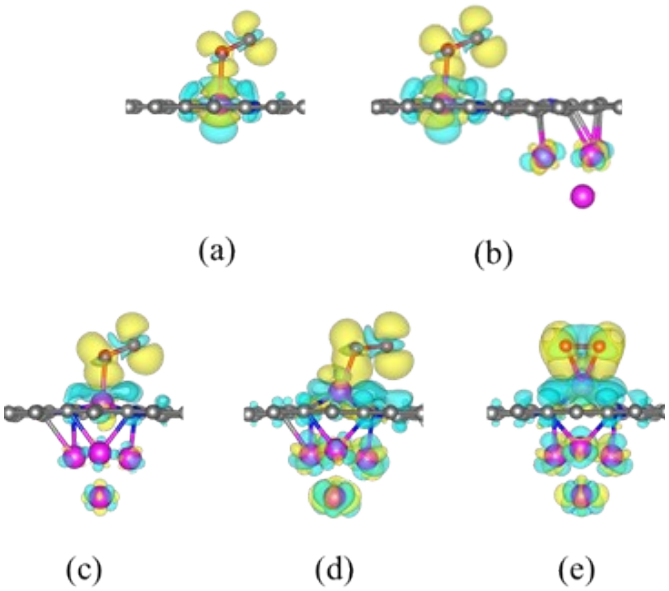

Figure S28. Charge density difference for O_2 adsorption at (a) the CoN_4, (b) the Co_4(Cg)-CoN_4, (c) in the end-on configuration at the Co_4-CoN_4 of low spin state, (d) in the end-on configuration at the Co_4-CoN_4 of high spin state, (e) in the side-on configuration at the Co_4-CoN_4, respectively. The isosurface level is 0.0015. The cyan and yellow regions represent charge density depletion and accumulation, respectively.

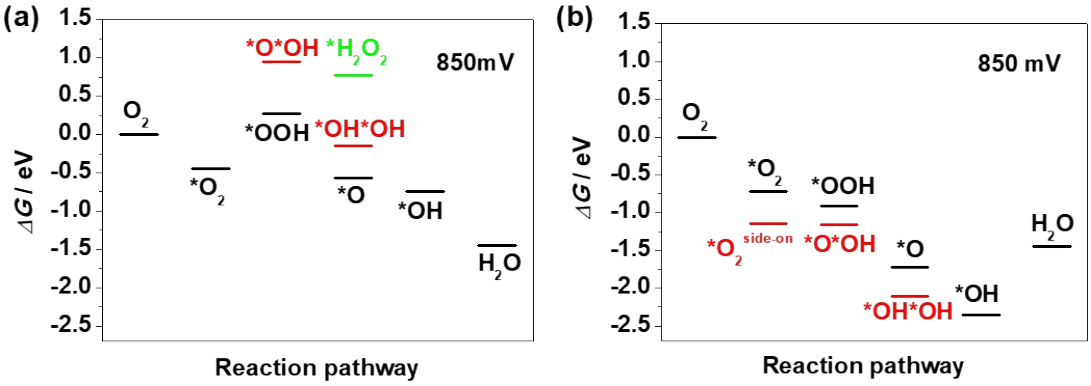

Figure S29. Free energy diagrams on ORR at (a) the CoN_4 and (b) the Co_4-CoN_4 structures. The O_2 adsorption at the high spin Co center of the Co_4-CoN_4 in the end-on and the side-on configurations were marked in black and red, respectively, and * indicates the Co center of the structures.

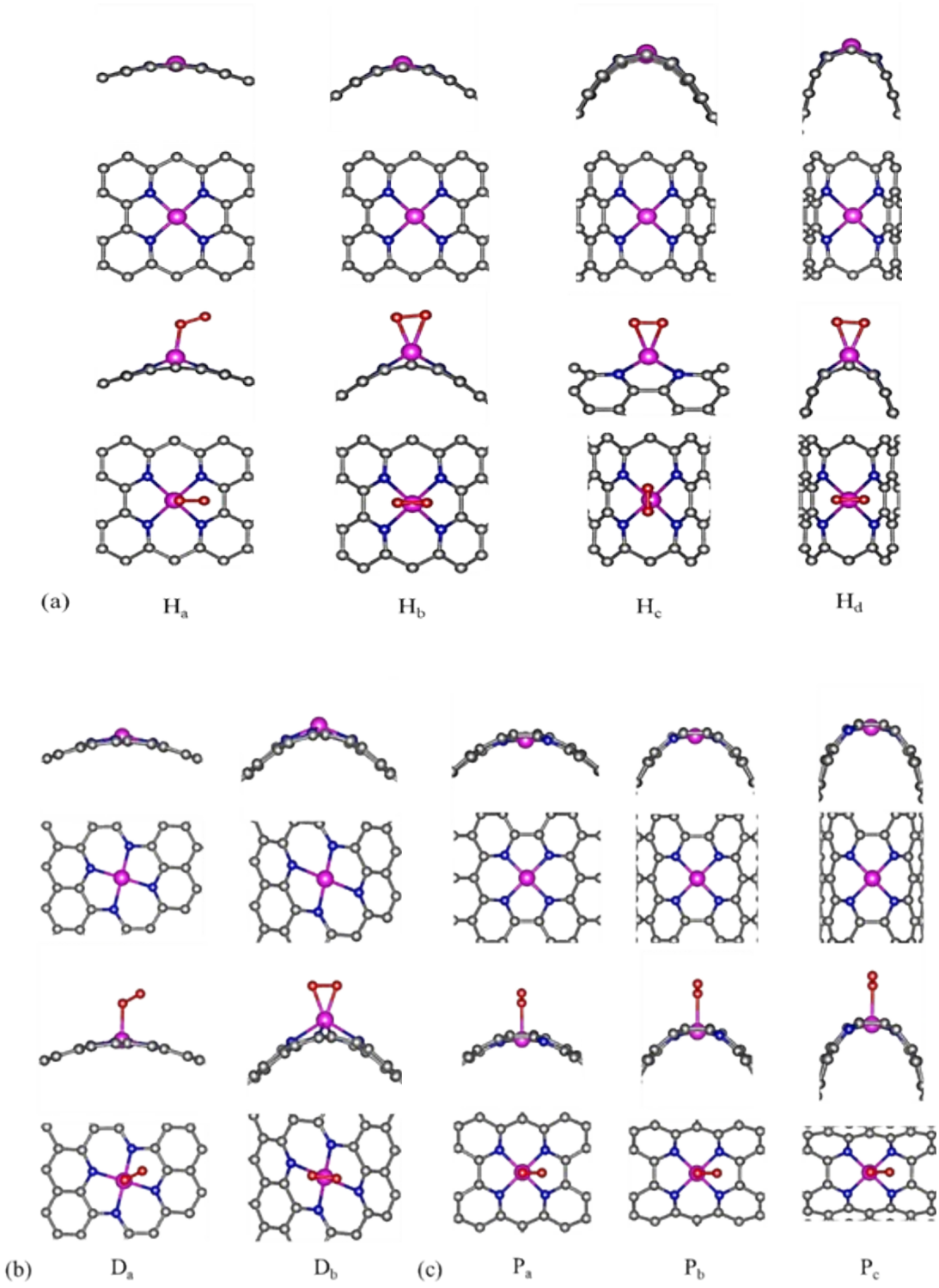

Figure S30. Top and side views of the CoN_4 structures and the corresponding O_2 adsorption configurations crinkling along the axis (a) H, (b) D and (c) P, respectively.

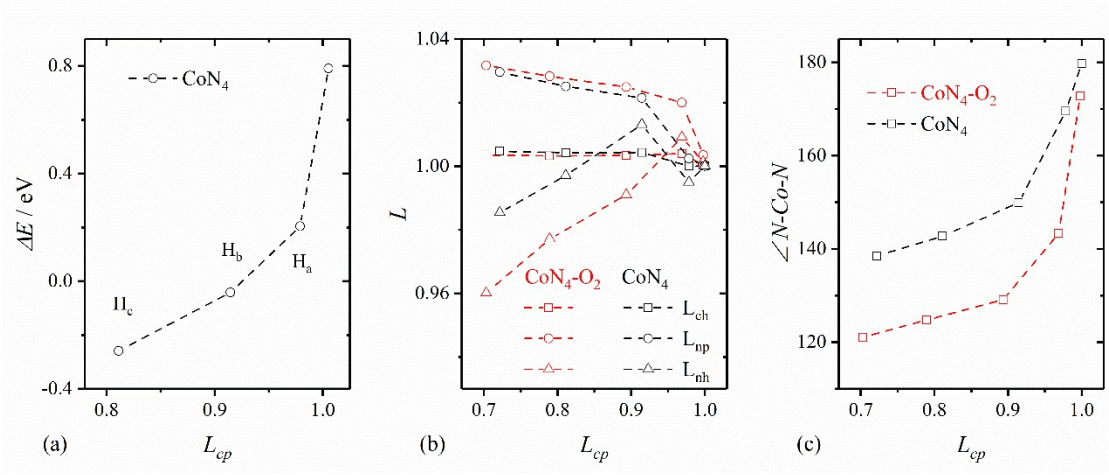

Figure S31. (a) Energy difference between the high spin and the low spin states of the CoN_4 structure crinkling along the axis H; (b) normalized distances L_{ch}, L_{np} and L_{nh} as a function of L_{cp} in the deformed CoN_4; (c) variation of the diagonal N-Co-N angles along the CoN_4 structure crinkling.

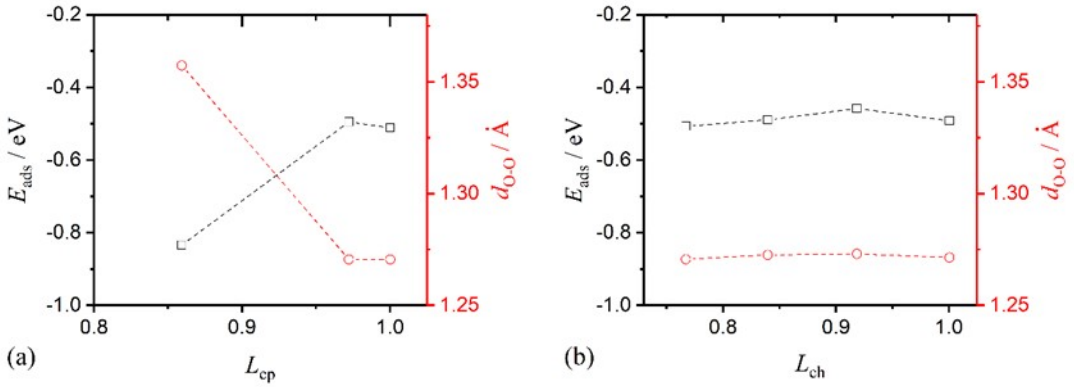

Figure S32. O_2 adsorption energy and the O-O bond length for the CoN_4 structure crinkling along the axis (a) D and (b) P, respectively.

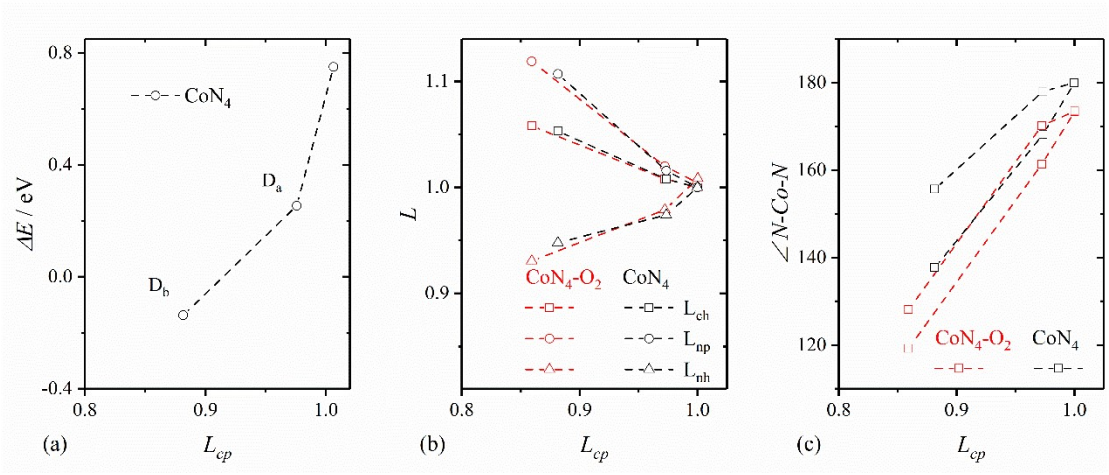

Figure S33. (a) Energy difference between the high spin and the low spin states of the CoN_4 structure crinkling along the axis D; (b) normalized distances L_{ch}, L_{np} and L_{nh} as a function of L_{cp} in the deformed CoN_4; (c) variation of the diagonal N-Co-N angles along the CoN_4 structure crinkling.

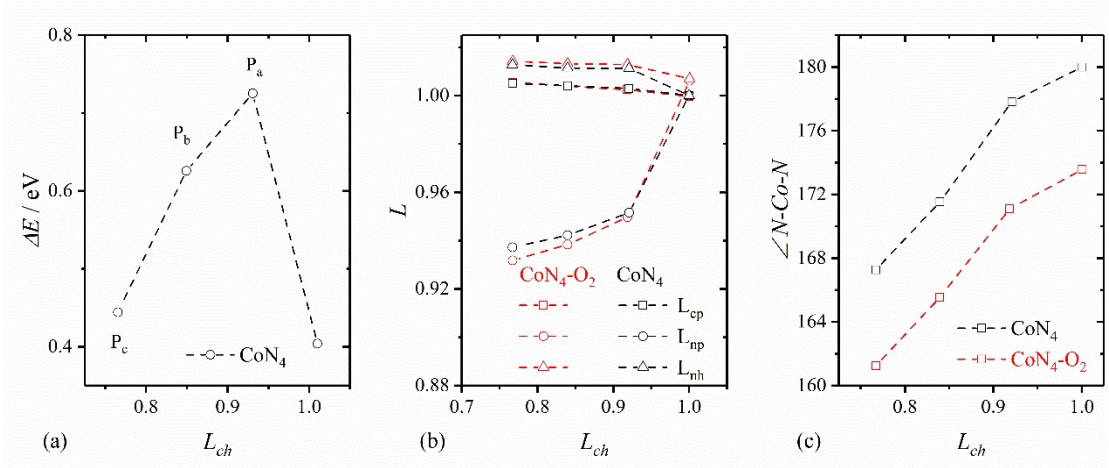

Figure S34. (a) Energy difference between the high spin and the low spin states of the CoN_4 structure crinkling along the axis P; (b) normalized distances L_{cp}, L_{np} and L_{nh} as a function of L_{ch} in the deformed CoN_4; (c) variation of the diagonal N-Co-N angles along the CoN_4 structure crinkling.

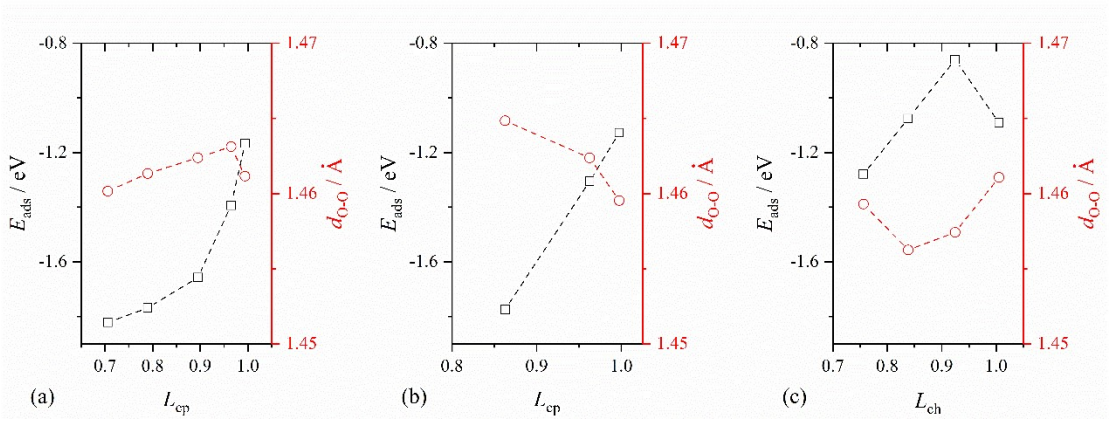

Figure S35. OOH adsorption energy and the O-O bond length of the CoN_4 structure crinkling along the axis (a) H, (b) D and (c) P, respectively.

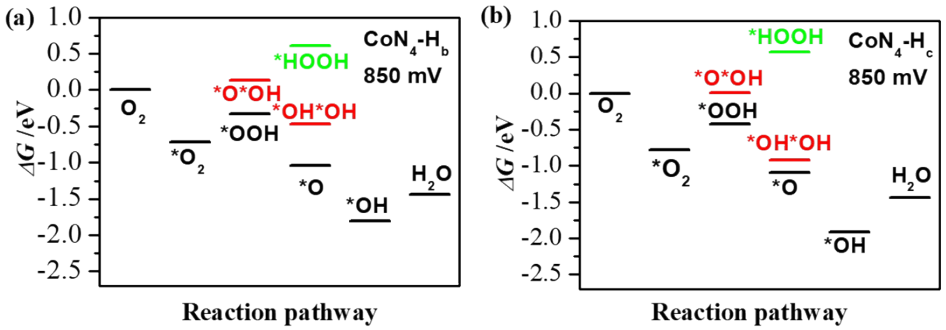

Figure S36. Free energy diagrams on ORR at the deformed CoN_4 structures (a) H_b and (b) H_c. The O_2 adsorption configuration is shown in Figure S30, and * indicates the Co center of the structures.

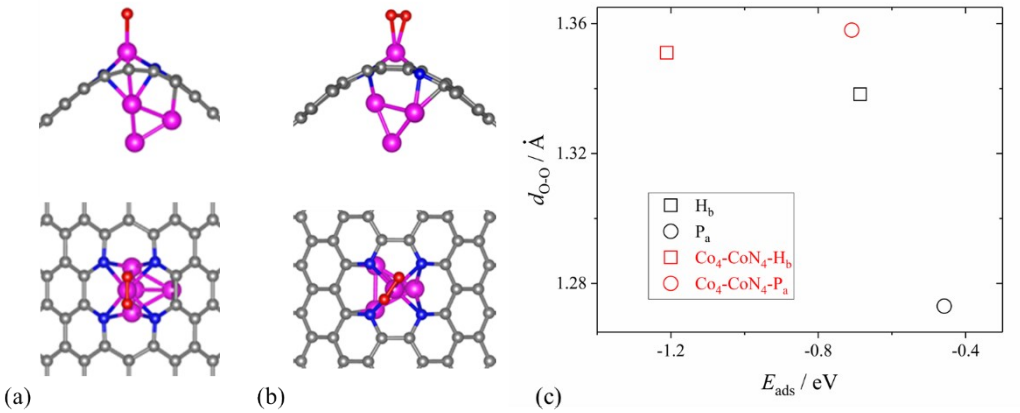

Figure S37. Top and side views of the deformed Co_4-CoN_4 structures corresponding to the (a) H_b and (b) the P_a, respectively.

Supplementary Tables

Table S1. Porosity of ZnCo-ZIF, Co_{NP}-N-C, *d*-(Co_{SA}-N-C) and *d*-(Co_{NP}/Co_{SA}-N-C) products.

Sample	S_{BET} (m^2 g^{-1})	S_{Micro} (m^2 g^{-1})	S_{meso}/S_{BET}	V_p (cm^3 g^{-1})
ZnCo-ZIF	1352.4	28.9	0.02	0.65
Co_{NP}-N-C	618.8	276.4	0.447	0.33
d-(Co_{SA}-N-C)	808.7	377.3	0.469	0.61
d-(Co_{NP}/Co_{SA}-N-C)	744.9	352.2	0.473	0.60

Table S2. XPS data for the surface species and ICP data for the bulk species of different catalysts.

Sample	ICP (wt.%) Co	XPS (at.%/wt.%) Co
Co_{NP}-N-C	2.72	1.31/5.90
d-(Co_{SA}-N-C)	2.59	1.06/4.83
d-(Co_{NP}/Co_{SA}-N-C) 20:1	2.95	-
d-(Co_{NP}/Co_{SA}-N-C) 10:1	3.97	1.26/5.56
d-(Co_{NP}/Co_{SA}-N-C) 5:1	4.66	-

Table S3. EXAFS fitting parameters at the Co K-edge for various samples（S_0^2=0.782）

	shell	CN	R(Å)	σ^2	ΔE_0	R factor
Co foil	Co-Co	12	2.49	0.0061	6.40	0.0022
Co	Co-N	3.4±0.2	1.99	0.0192	1.25	0.0171
	Co-Co	0.9±0.2	2.48	0.0059		

Table S4. Comparison of ORR performance of *d*-(Co_{NP}/Co_{SA}-N-C) with other reported M-N-C catalysts.

Catalysts	**Catalyst loading (mg cm^{-2})**	E_{onset} **(V vs.RHE)**	$E_{1/2}$ **(V vs.RHE)**	**Ref.**
***d*-(Co_{NP}/Co_{SA}-N-C)**	**0.800**	**0.950**	**0.830**	**This work**
C-FeZIF-1.44-950	0.500	0.910	0.780	[11]
SA-Fe-N	0.600	0.980	0.812	[12]
$FeCoN_X$/C	0.400	1.020	0.860	[13]
20Mn-NC-second	0.800	-	0.800	[14]
Co–N–C@F127	0.800	0.930	0.840	[15]
Fe1-N-NG/RGO	0.600	0.960	0.840	[16]
Cr/N/C	-	-	0.773	[17]
FeSA–N–C	0.280	-	0.800	[18]
Co–N–PCNF	0.800	0.950	0.810	[19]

Table S5. Comparison of H_2-O_2 PEMFC performance of *d*-(Co_{NP}/Co_{SA}-N-C) with other reported M-N-C catalysts.

Catalysts	Catalyst loading (mg cm^{-2})	Back pressure	P_{max} ($W \cdot cm^{-2}$)	Ref.
***d*-(Co_{NP}/Co_{SA}-N-C)**	**4.0**	**2.0 bar** **1.0 bar**	**1.207** **1.060**	**This work**
C-FeZIF-1.44-950	1.0	30 psi	0.775	[11]
Fe–N/CNT-2	4.0	1.5 bar	0.360	[20]
1MIL/40ZIF-1000	4.0	1.0 bar	0.760	[21]
20Mn-NC-second	4.0	1.0 bar	0.460	[14]
TPI@Z8(SiO_2)-650-C	2.7	2.5 bar	1.180	[22]
H-Fe-Nx-C	2.0	29.4 psi	0.710	[23]
Co–N–C@F127	4.0	1.0 bar	0.870	[15]
HC-5Co95Zn	4.0	-	0.412	[24]
HP-FeN_4	4.0	2.0 bar	0.700	[25]
20Co-NC-1100	4.0	30 psi	0.560	[26]
FeSA–N–C	3.0	1.5 bar	0.680	[18]
Co–N–PCNF	4.0	1.0 bar	0.710	[19]

Table S6. Comparison of H_2-air PEMFC performance of *d*-(Co_{NP}/Co_{SA}-N-C) with other reported M-N-C catalysts.

Catalysts	Catalyst loading (mg cm^{-2})	Back pressure	P_{max} ($W \cdot cm^{-2}$)	Ref.
***d*-(Co_{NP}/Co_{SA}-N-C)**	4.0	1.0 bar	0.454	**This work**
C-FeZIF-1.44-950	1.0	30 psi	0.463	[11]
TPI@Z8(SiO2)-650-C	2.0	1.0 bar	0.420	[22]
H-Fe-Nx-C	2.0	29.4 psi	0.2-0.225	[23]
Co–N–C@F127	4.0	1.0 bar	0.270	[15]
20Co-NC-1100	4.0	30 psi	0.280	[26]
Co–N–PCNF	4.0	1.0 bar	0.400	[19]

Table S7. Summary of the previously reported durability of M-N-C catalysts in RDE and MEA.

Catalysts	$E_{1/2}$ (Vvs.RHE)	H_2/O_2, P_{max} ($W \cdot cm^{-2}$)	MA loss in RDE	MA loss in MEA	Ref.
***d*-(Co_{NP}/Co_{SA}-N-C)**	**~0.83**	**~1.27 (2.0 bar, 80°C)**	**~12 mV (50000 cycles)**	**~39% (0.5V100H) ~51.4% (0.6V100H)**	**This work**
C-FeZIF-1.44-950	~0.78	~0.46 (1.0 bar, 80°C)	~10% (1A, 20000s)	~32% (1A, 10h)	11
HP-FeN_4	~0.80	~0.70 (2.0 bar, 80°C)	~26 mV (10000 cycles)	~52% (0.6V, 50h)	25
Fe–N/CNT-2	~0.78	~0.36 (1.5 bar, 80°C)	~20 mV (500 cycles)	~70% (0.7V, 30h)	20
0.17CVD/Fe-N-C-kat	~0.84	~0.70 (1.0 bar, 80°C)	~35 mV (50000 cycles)	~45.7% (0.7V, 100h)	27
Co(mIm)–NC(1.0)	~0.82	~0.64 (1.0 bar, 80°C)	~8 mV (10000 cycles)	~20.5% (0.7V, 100h)	28
TPI@Z8(SiO_2)-650-C	Not given	~1.18 (2.5 bar, 80°C)	Not given	~40% (0.5V, 20h)	22
20Mn-NC-second	~0.80	~0.46 (1.0 bar, 80°C)	~17 mV (30000 cycles)	~43% (0.7V, 100h)	14
20Co-NC-1100	~0.80	~0.55 (2.0 bar, 80°C)	~30 mV (10000 cycles)	~62% (0.7V, 100h)	26
Fe2-Z8-C	~0.81	~1.14 (2.5 bar, 80°C)	~1.8% (0.5V, 10000s)	~87% (0.5V, 50h)	9
Fe/N/C(4mlm)-OAc	~0.84	~1.33 (2.0 bar, 80°C)	Not given	~80.3% (0.5V, 35h)	29

FeN4/HOPC-c-1000	~0.80	~0.69 (1.0 bar, 80°C)	~17% (0.8V, 24h)	~47% (0.55V, 100h)	30

Table S8. Co magnetic moment and electronic energy difference ($\Delta E = E_{high} - E_{low}$, eV) between low and high spin states of the CoN_4 and Co_4-CoN_4 structures at different Hubbard U values.

	U_h	low	high	ΔE
CoN_4	3.1	1.011	2.624	0.930
	4.2	1.028	2.656	0.584
	4.9	1.036	2.691	0.400
	5.3	1.039	2.711	0.324
Co_4-CoN_4	3.1	0.794	2.441	0.415
	4.2	0.801	2.550	0.171
	4.9	0.894	2.604	0.058
	5.3	0.911	2.594	-0.011

Table S9. O_2 adsorption energy (E_{ads}, eV) and the O-O bond length (d, Å) for the CoN_4 structure at the low spin and the high spin states.

CoN_4	U_h	E_{ads}	d
low spin (end-on)	3.1	-0.540	1.275
	4.2	-0.496	1.272
	4.9	-0.482	1.270
	5.3	-0.477	1.269
high spin (end-on)	3.1	0.059	1.295
	4.2	-0.120	1.293
	4.9	-0.251	1.293
	5.3	-0.327	1.293
high spin (side-on)	3.1	0.280	1.391
	4.2	0.203	1.380

	4.9	0.120	1.365
	5.3	-0.062	1.336

Table S10. O_2 adsoprtion energy (E_{ads}, eV) and the O-O bond length (d, Å) for the Co_4-CoN_4 structure at the low spin and the high spin states.

Co_4-CoN_4	U_h	E_{ads}	d
low spin (end-on)	3.1	-0.922	1.297
	4.2	-0.831	1.291
	4.9	-0.736	1.287
	5.3	-0.711	1.286
high spin (side-on)	3.1	-1.085	1.400
	4.2	-1.169	1.407
	4.9	-1.202	1.406
	5.3	-1.243	1.405
high spin (end-on)	3.1	-0.797	1.319
	4.2	-1.019	1.321
	4.9	-1.119	1.322
	5.3	-1.183	1.323

Table S11. O_2 adsorption energy (E_{ads}, eV), the O-O bond length (d, Å) and Co magnetic moment (u) at U_h = 4.9 for the relevant CoN_4 structures.

	configuration	E_{ads}	d	u
CoN_4	end-on (low spin, S1)	-0.482	1.270	0.924
$Co_4(C_g)$-CoN_4	end-on (low spin, S2)	-0.515	1.275	0.930
	end-on (high spin)	-0.375	1.301	2.612
	side-on (high spin)	-0.192	1.332	2.653
Co_4-CoN_4	side-on (high spin, S3)	-1.202	1.406	2.212
	end-on (high spin, S4)	-1.119	1.322	2.565
	end-on (low spin, S5)	-0.736	1.287	0.580

Table S12. Partial charges of the O atoms for O_2 adsorption at the Co center at U_h = 4.9 eV for different CoN_4 structures based on the Bader population analysis. The O atom that bonds to the Co center is more negative in the end-on pattern.

	configureaton	q	
gas		-0.007	0.007
CoN_4	end-on (low spin)	-0.139	-0.161
Co_4(Cg)-CoN_4	end-on (low spin)	-0.075	-0.259
Co_4-CoN_4	side-on (high spin)	-0.310	-0.484
	end-on (high spin)	-0.226	-0.361
	end-on (low spin)	-0.128	-0.228

Table S13. O_2 dissociation barriers (E_a, eV) at U_h = 4.9 eV for the corresponding CoN_4 structures.

	configuration	E_a
CoN_4	end-on (low spin)	2.38
	side-on (high spin)	2.43
$Co_4(C_g)$-CoN_4	end-on (low spin)	1.52
	side-on (high spin)	1.79
Co_4-CoN_4	end-on (high spin)	0.85
	side-on (high spin)	1.45

Table S14. OOH adsorption energy (E_{ads}, eV), the O-O bond length (d, Å) and Co center magnetic moment (u) at Uh = 4.9 eV for the relevant CoN_4 structures.

	E_{ads}	d	u
CoN_4	-1.076	1.458	2.576
	-0.940	1.418	0.813
$Co_4(C_g)$-CoN_4	-1.234	1.466	2.603
	-0.899	1.427	1.010
Co_4-CoN_4	-2.226	1.481	2.595
	-1.306	1.456	0.871

Table S15. OOH dissociation barriers (E_a, eV) at U_h = 4.9 eV for the relevant CoN_4 structures.

	mechanism	E_a
CoN_4	M1	0.96
	M2	1.20
$Co_4(C_g)$-CoN_4	M1	0.93
	M2	1.03
Co_4-CoN_4	M1	0.69

Supplementary References

1. X. D. H. Chao L, Jing W, Hao S, Yan N Y, Yang L, Jian S L, and C. Z. Y. Lian J W, *Adv. Funct. Mater*, 2018, **28**, 1705253.
2. Z. Wang, W. Xu, X. Chen, Y. Peng, Y. Song, C. Lv, H. Liu, J. Sun, D. Yuan, X. Li, X. Guo, D. Yang and L. Zhang, *Adv. Funct. Mater.*, 2019, **29**, 1902875.
3. G. Kresse, *Phys. Rev*, 1996, **54**, 11169.
4. K. B. John P. Perdew, Matthias Ernzerhof, *Phys. Rev. Lett.*, 1996, **77**, 3865.
5. S. Grimme, S. Ehrlich and L. Goerigk, *J Comput Chem*, 2011, **32**, 1456-1465.
6. G. A. B. S. L. Dudarev, S. Y. Savrasov, C. J. Humphreys, A. P. Sutton, *Phys. Rev*, 1998, **57**, 1505.
7. A. Heyden, A. T. Bell and F. J. Keil, *J Chem Phys*, 2005, **123**, 224101.
8. A. Kulkarni, S. Siahrostami, A. Patel and J. K. Norskov, *Chem Rev*, 2018, **118**, 2302-2312.
9. Q. Liu, X. Liu, L. Zheng and J. Shui, *Angew. Chem. Int. Ed.*, 2018, **57**, 1204-1208.
10. Y. C. W. Chao Zhang, Bing An, Ruiyun Huang, Cheng Wang, Zhiyou Zhou, Wenbin Lin, *Adv. Mater.*, 2017, **29**, 1604556.
11. Y. Deng, B. Chi, J. Li, G. Wang, L. Zheng, X. Shi, Z. Cui, L. Du, S. Liao, K. Zang, J. Luo, Y. Hu and X. Sun, *Adv. Energy Mater.*, 2019, **9**, 1802856.
12. Z. Miao, X. Wang, M. C. Tsai, Q. Jin, J. Liang, F. Ma, T. Wang, S. Zheng, B. J. Hwang, Y. Huang, S. Guo and Q. Li, *Adv. Energy Mater*, 2018, **8**, 1801226.
13. M. Xiao, Y. Chen, J. Zhu, H. Zhang, X. Zhao, L. Gao, X. Wang, J. Zhao, J. Ge, Z. Jiang, S. Chen, C. Liu and W. Xing, *J. Am. Chem. Soc.*, 2019, **141**, 17763-17770.
14. M. J. C. Jia Z L, David A. Cullen, Sooyeon Hwang, Mao Y W, Bo Y L, Ke X L,, M. L. Stavros Karakalos, Han G Z, Chao L, Hui X, George E. Sterbinsky, and D. S. Zhen X F, Karren L. More, Guo F W, Zhen B W Gang W *Nat. Catal.*, 2018, **1**, 935–945.
15. Y. He, S. Hwang, D. A. Cullen, M. A. Uddin, L. Langhorst, B. Li, S. Karakalos, A. J. Kropf, E. C. Wegener, J. Sokolowski, M. Chen, D. Myers, D. Su, K. L. More, G. Wang, S. Litster and G. Wu, *Energy Environ. Sci.*, 2019, **12**, 250-260.
16. Q. Shao, C. Nianji Zhang , Claudia W. Narvaez Villarrubia, Xiang Huang, Lin Xie, and X. K. Xiyang Wang, Hu Xu, Gang Wu, Jie Zeng, Hsing-Lin Wang*, *Nano Energy*, 2019, **66**, 104164.
17. E. Luo, H. Zhang, X. Wang, L. Gao, L. Gong, T. Zhao, Z. Jin, J. Ge, Z. Jiang, C. Liu and W. Xing, *Angew. Chem. Int. Ed.*, 2019, **58**, 12469-12475.
18. R. Z. Long Jiao, Gang Wan, Weijie Yang, Xin Wan, Hua Zhou, Jianglan Shui, and S.-H. Y. H.-L. Jiang, *Nat. Commun.*, 2020, **11**, 2831.
19. Y. He, H. Guo, S. Hwang, X. Yang, Z. He, J. Braaten, S. Karakalos, W. Shan, M. Wang, H. Zhou, Z. Feng, K. L. More, G. Wang, D. Su, D. A. Cullen, L. Fei, S. Litster and G. Wu, *Adv. Mater.*, 2020, **32**, 2003577.
20. D. Xia, X. Yang, L. Xie, Y. Wei, W. Jiang, M. Dou, X. Li, J. Li, L. Gan and F. Kang, *Adv. Funct. Mater*, 2019, **29**, 1906174.
21. H. Wang, F. X. Yin, N. Liu, R. H. Kou, X. B. He, C. J. Sun, B. H. Chen, D. J. Liu and H. Q. Yin, *Adv. Funct. Mater*, 2019, **29**, 1901531.
22. X. Wan, X. Liu, Y. Li, R. Yu, L. Zheng, W. Yan, H. Wang, M. Xu and J. Shui, *Nat. Catal.*, 2019, **2**,

259-268.

23. H. Yang, X. Chen, W. T. Chen, Q. Wang, N. C. Cuello, A. Nafady, A. M. Al-Enizi, G. I. N. Waterhouse, G. A. Goenaga, T. A. Zawodzinski, P. E. Kruger, J. E. Clements, J. Zhang, H. Tian, S. G. Telfer and S. Ma, *ACS Nano*, 2019, **13**, 8087-8098.
24. Z. Meng, S. Cai, R. Wang, H. Tang, S. Song and P. Tsiakaras, *Appl Catal B- Environ* 2019, **244**, 120-127.
25. N. Zhang, T. Zhou, M. Chen, H. Feng, R. Yuan, C. a. Zhong, W. Yan, Y. Tian, X. Wu, W. Chu, C. Wu and Y. Xie, *Energy Environ. Sci.*, 2020, **13**, 111-118.
26. D. A. C. Xiao Xia Wang, Yung-Tin Pan, Sooyeon Hwang, Maoyu Wang,, J. W. Zhenxing Feng, Mark H. Engelhard, Hanguang Zhang, Yanghua He, and D. S. Yuyan Shao, Karren L. More, Jacob S. Spendelow,* and Gang Wu*, *Adv. Mater.*, 2018, **30**, 1706758.
27. S. Liu, M. W. , X. Y. , Q. S. , Zhi Qiao, Marcos Lucero, and K. L. M. Qing Ma, David A. Cullen, Zhenxing Feng, Gang Wu, *Angew. Chem. Int. Ed.*, 2020, **59**, 2-10.
28. C. H. Xiaohong Xie , Boyang Li, Yanghua He , David A. Culle , Evan C. Wegener, , U. M. A. Jeremy Kropf , Yingwen Cheng, Mark H. Engelhard , Mark E. Bowden, , T. L. Miao Song, Xiaohong S. Li, Zimin Nie, Jian Liu, Deborah J. Myers, and G. W. Piotr Zelenay , Gang Wu , Vijay Ramani , Yuyan Shao, *Nat. Catal.*, 2020, **3**, 1044–1054.
29. Y. Li, P. Zhang, L. Wan, Y. Zheng, X. Qu, H. Zhang, Y. Wang, K. Zaghib, J. Yuan, S. Sun, Y. Wang, Z. Zhou and S. Sun, *Adv. Funct. Mater.*, 2021, **31**, 2009645.
30. M. Qiao, Y. Wang, Q. Wang, G. Hu, X. Mamat, S. Zhang and S. Wang, *Angew. Chem. Int. Ed.* , 2020, **59**, 2688-2694.